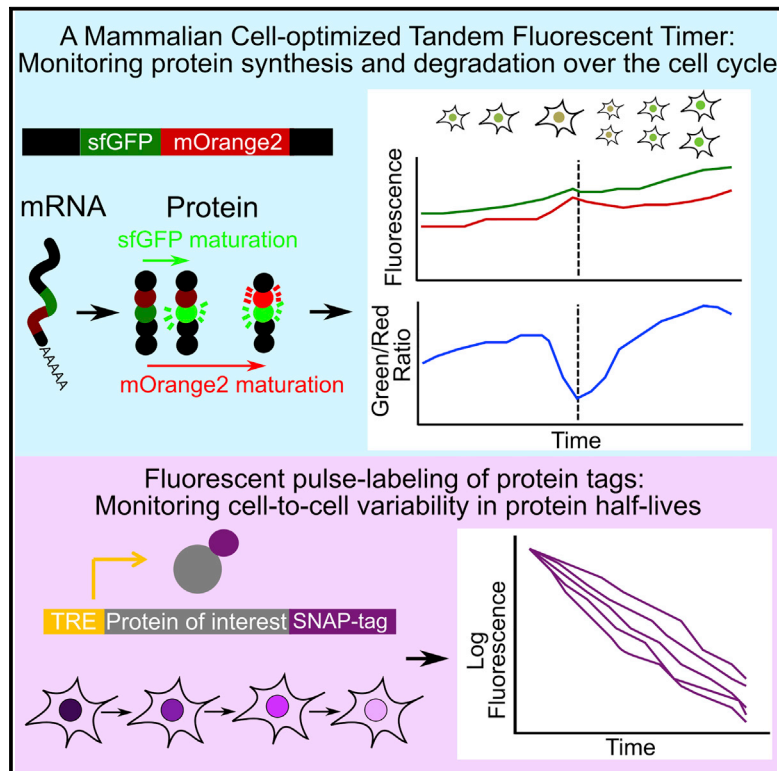


# Molecular Cell

## Single Live Cell Monitoring of Protein Turnover Reveals Intercellular Variability and Cell-Cycle Dependence of Degradation Rates

### Graphical Abstract



### Authors

Andrea Brigitta Alber,  
Eric Raphael Paquet, Martina Biserni,  
Felix Naef, David Michael Suter

### Correspondence

david.suter@epfl.ch

### In Brief

Alber et al. developed a method allowing disentangling protein synthesis and degradation in live cells. They found ~40% of proteins to be stabilized during cell division, large and global intercellular variability in protein degradation rates, and correlated synthesis and degradation rates in individual cells to buffer protein expression variability.

### Highlights

- A fluorescent timer to disentangle protein synthesis and degradation in live cells
- ~40% of proteins are stabilized during mitosis
- Half-lives of different proteins co-vary within single cells
- Protein degradation and synthesis rates are positively correlated in single cells

# Single Live Cell Monitoring of Protein Turnover Reveals Intercellular Variability and Cell-Cycle Dependence of Degradation Rates

Andrea Brigitta Alber,<sup>1,2</sup> Eric Raphael Paquet,<sup>1,2</sup> Martina Biserni,<sup>1</sup> Felix Naef,<sup>1</sup> and David Michael Suter<sup>1,3,\*</sup>

<sup>1</sup>Institute of Bioengineering, School of Life Sciences, Ecole Polytechnique Fédérale de Lausanne (EPFL), Lausanne 1015, Switzerland

<sup>2</sup>These authors contributed equally

<sup>3</sup>Lead Contact

\*Correspondence: [david.suter@epfl.ch](mailto:david.suter@epfl.ch)

<https://doi.org/10.1016/j.molcel.2018.07.023>

## SUMMARY

Cells need to reliably control their proteome composition to maintain homeostasis and regulate growth. How protein synthesis and degradation interplay to control protein expression levels remains unclear. Here, we combined a tandem fluorescent timer and pulse-chase protein labeling to disentangle how protein synthesis and degradation control protein homeostasis in single live mouse embryonic stem cells. We discovered substantial cell-cycle dependence in protein synthesis rates and stabilization of a large number of proteins around cytokinesis. Protein degradation rates were highly variable between cells, co-varied within individual cells for different proteins, and were positively correlated with synthesis rates. This suggests variability in proteasome activity as an important source of global extrinsic noise in gene expression. Our approach paves the way toward understanding the complex interplay of synthesis and degradation processes in determining protein levels of individual mammalian cells.

## INTRODUCTION

Dynamic changes in protein expression levels are determined by how cells balance the rates at which proteins are synthesized and degraded. In proliferating cells, the proteome needs to be precisely doubled from one division to the next, as otherwise cell homeostasis would be compromised. However, how doubling of global protein levels is achieved and how protein synthesis and degradation rates vary over the cell cycle is not well understood. Studies based on transcriptome and proteome-wide approaches, such as ribosome profiling or puromycin-associated nascent chain proteomics (PUNCH-P), have reported that most proteins are synthesized at similar relative rates in G1, S, and G2 phase (Aviner et al., 2013; Stumpf et al., 2013; Tanenbaum et al., 2015). Larger changes in protein synthesis occur in M phase, during which transcriptional activity (Palozola et al., 2017; Parsons and Spencer, 1997) and transla-

tional efficiency of most mRNAs are strongly reduced (Tanenbaum et al., 2015). In contrast, our understanding on changes in protein degradation rates over the cell cycle is restricted to specific cases such as proteins involved in cell-cycle regulation (Shaik et al., 2012) and targets of the GSK3 kinase (Acebron et al., 2014). Furthermore, most of these studies are limited by low temporal resolution, the use of cell-cycle synchronizing drugs that can interfere with translation (Coldwell et al., 2013), and cell population-based measurements that obscure cell-to-cell variability.

Over the past decade, single-cell analysis has revealed surprisingly large intercellular variability in gene expression, which has direct implications on a broad range of biological processes (Kaern et al., 2005; Raj and van Oudenaarden, 2008). This is of particular relevance for stem cells, as expression level variability of certain stem cell markers can have an impact on cell differentiation (Chang et al., 2008). Importantly, variability in gene transcription was shown to vary substantially between genes (Suter et al., 2011), however, it is not known whether this is also true for downstream steps of gene expression such as translation and protein degradation.

Here, we leveraged on several single-cell time-lapse imaging strategies and computational modeling to disentangle synthesis and degradation rates of 40 endogenous proteins in mouse embryonic stem cells (ESCs) and to measure cell-to-cell variability in protein turnover. First, we developed an approach based on protein tagging with a tandem fluorescent timer and show that it allows for simultaneously measuring synthesis and degradation rates of endogenous proteins in single ESCs. Second, we used pulse-chase labeling and time-lapse imaging of dual fluorescent SNAP/Halo-tags to measure protein degradation rates in individual cells. We found that protein synthesis varies substantially between G1 and G2 phase, while degradation is markedly decreased for a large fraction of proteins around cytokinesis. Surprisingly, protein degradation rates displayed significant intercellular variability in both ESCs and fibroblasts and these were accompanied by compensatory changes in protein synthesis rates that dampened intercellular variability in protein expression levels. Finally, we show that cell-to-cell variability in protein degradation rates is caused by global rather than gene-specific differences in protein degradation and is correlated with single-cell expression levels of the proteasome component ADRM1.

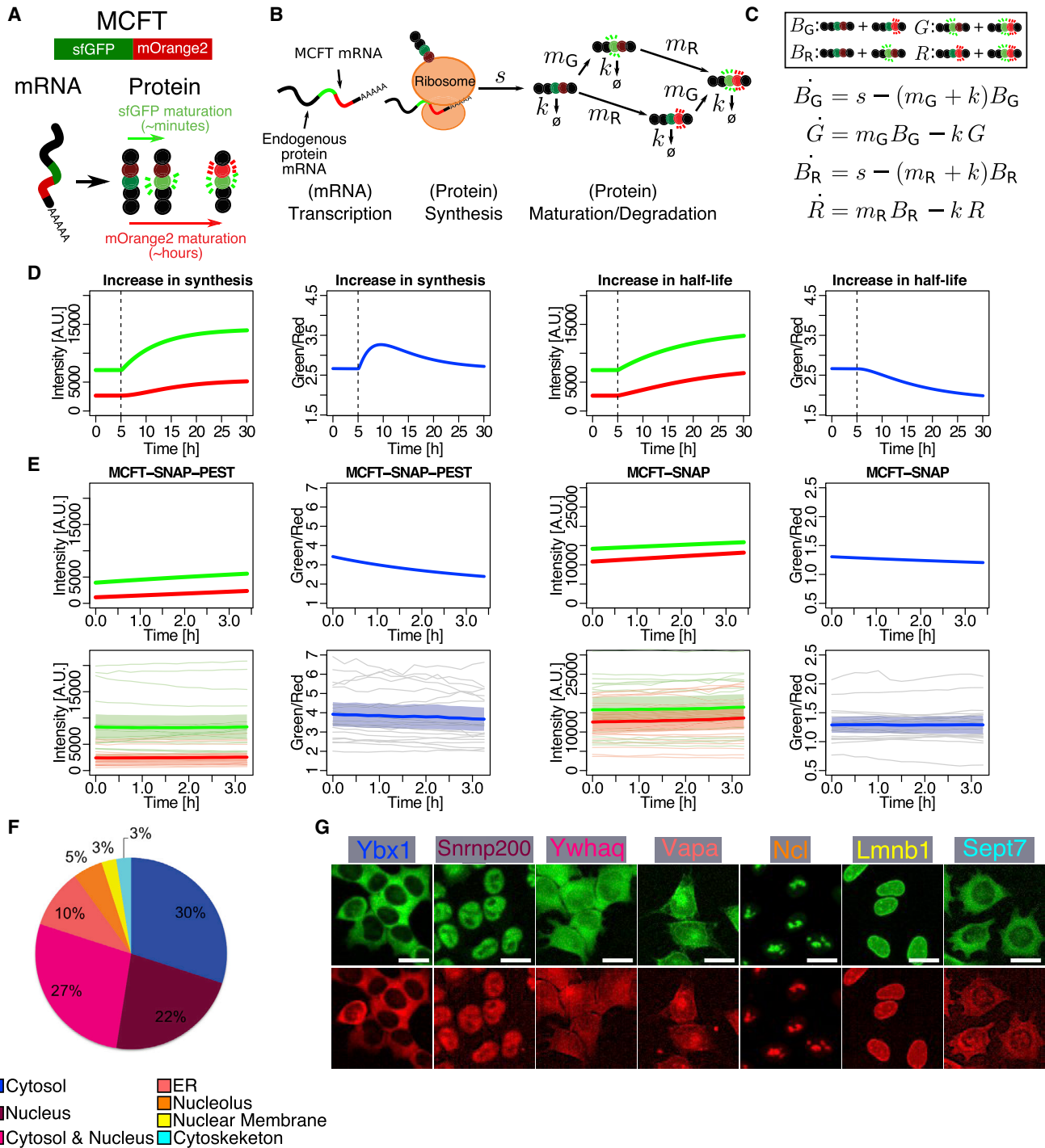


**Figure 1. Characterization of the MCFT and MCFT-Tagged Protein Library**

(A) Description of the mammalian cell-optimized fluorescent timer (MCFT). The timer is composed of a green fluorescent protein (sfGFP) with a fast maturation time (in the range of minutes) and a red fluorescent protein (mOrange2) with a longer maturation time (in the range of several hours).

(B) Our model of the MCFT assumes that sfGFP and mOrange2 mature independently at rates  $m_G$  and  $m_R$ , and that degradation of the full polypeptide is independent on the maturation state of either fluorophore.  $s$ , synthesis rate;  $B_G$ , immature (black) form of sfGFP;  $G$ , mature form of sfGFP;  $B_R$ , immature (black) form of mOrange2;  $R$ , mature form of mOrange2;  $k$ , degradation rate of the MCFT;  $m_G$ , maturation rate of sfGFP;  $m_R$ , maturation rate of mOrange2.

(C) The MCFT is modeled using a set of four differential equations describing the model presented in (B).

(D) Simulations of fluorescence intensity changes upon changes of MCFT synthesis or degradation, using maturation half-times of 5 min for sfGFP and 510 min for mOrange2.

(legend continued on next page)

## RESULTS

### A Mammalian-Cell-Optimized Tandem Fluorescent Timer to Monitor Endogenous Protein Turnover in Single Cells

Tandem fluorescent timers consist of the fusion of a fast-maturing superfolder green fluorescent protein (sfGFP) to a slower maturing red fluorescent protein (Khmelniskii et al., 2012). The distinct maturation times of the two fluorophores can be used to measure protein age and stability. While a mCherry fusion to sfGFP is ideal to study shorter-lived yeast proteins, mammalian proteins are longer lived and thus require a red fluorescent protein with a longer maturation half-time (Figure S1A). Therefore, we decided to use a fusion of sfGFP and mOrange2, hereafter named mammalian-cell-optimized fluorescent timer (MCFT), because mOrange2 has a maturation time of several hours (Figures 1A and S1A) (Shaner et al., 2008).

While tandem fluorescent timers have been mainly used as a readout of protein age or to compare relative degradation rates between different proteins (Khmelniskii et al., 2014), we reasoned that they could also allow distinguishing between dynamic changes in protein synthesis and protein degradation because these processes should impact differently on changes in the emission of the two fluorophores. To substantiate this concept, we performed computational simulations of fluorescence time traces of the MCFT, subjected to shifts in synthesis and degradation rates (Figures 1B–1D). We simulated the MCFT using a set of four differential equations corresponding to the four protein states of our MCFT, i.e., the immature and mature forms of both the sfGFP and mOrange2 fluorophores (Figures 1B and 1C; STAR Methods). While similar changes in steady-state protein levels can be obtained by opposite alterations of synthesis or degradation rates, these two scenarios will reflect differently on the ratio between green and red fluorescence (Figure 1D). Therefore, time-lapse monitoring of the MCFT should enable disentangling changes in protein synthesis versus protein degradation. As a proof of principle to illustrate this, we simulated fluorescence levels using the model (including realistic levels of noise; see STAR Methods) and fitted those traces, which showed that synthesis and degradation rates could be retrieved accurately from the combined green and red time traces, even in a non-steady-state configuration (Figures S1B and S1C; STAR Methods).

To complement our simulations and to confirm that indeed the MCFT is sensitive to protein half-lives, we generated two mouse ESC lines allowing doxycycline (dox)-inducible expression of a nuclear MCFT or a nuclear MCFT fused to a protein destabilization sequence (PEST), respectively (Rogers et al., 1986). In addition, we fused both MCFT versions to a SNAP-tag (Keppler et al., 2003), allowing quantification of protein half-lives *in vivo* (Alber and Suter, 2018; Bojkowska et al., 2011) (Figure S1D).

We then determined the half-lives of MCFT-SNAP-PEST and MCFT-SNAP by pulse-labeling with SNAP SiR-647 ligand 24 hr after dox induction, followed by fluorescence decay monitoring by microscopy ( $6.9 \pm 2.2$  hr [SD] and  $21.0 \pm 5.3$  hr [SD], respectively, Figure S1E). Next, we monitored green and red fluorescence time traces of MCFT-SNAP-PEST and MCFT-SNAP 48 hr after dox induction at the single-cell level (Figure 1E). As expected, and in line with our simulations, we observed a lower level of intensity of the sfGFP-mOrange2 fluorophores as well as a higher level for the green/red ratio for the MCFT-SNAP-PEST in comparison with the MCFT-SNAP (Figure 1E). Using the half-lives determined by the SNAP fluorescence decay, the experimental data could be well reproduced by simulations, suggesting that modeling the MCFT should enable inferring protein synthesis and degradation rates in mouse ESCs.

### A Library of Endogenously MCFT-Tagged Proteins

We next aimed at using the MCFT to monitor endogenous protein synthesis and degradation rates in single live cells. To do so, we took advantage of the central dogma (CD)-tagging approach (Jarvik et al., 1996), which allows for internal fusions of fluorescent tags to endogenous proteins in mammalian cells (Harikumar et al., 2017; Sigal et al., 2007), mostly without altering their turnover rates (Cohen et al., 2008). We generated a library of 40 mouse ESC lines, in each of which a different endogenous protein was tagged with the MCFT (Figure S1F) and identified by 3' rapid amplification of cDNA ends (3' RACE) (Yeku and Frohman, 2011). The 40 tagged proteins spanned a broad range of biological functions (Figure S1G; Table S1) and their subcellular localizations mostly (38/40) matched those described in the literature (Figures 1F and 1G; Table S1).

### Protein Accumulation Dynamics during Interphase

How protein synthesis and degradation interplay to control protein accumulation during the cell cycle is not well understood. To quantify protein accumulation, synthesis, and degradation over the cell cycle in single live cells, we measured the total nuclear green (sfGFP) and red (mOrange2) fluorescence intensities from one division to the next with time intervals of 15 min for 6 nuclear timer-tagged proteins from our library using semi-automated cell tracking. The temporal accumulation of the green fluorescence intensity, which is a good surrogate of the absolute protein level due to the short maturation time of the sfGFP (STAR Methods), showed that all protein levels steadily increased during the cell cycle (Figure 2A). In fact, none seemed to reach a steady state within one cell cycle, which likely reflects that the studied proteins are longer-lived than the cell-cycle duration ( $12.3 \pm 2$  hr [SD]). To estimate synthesis (*s*) and degradation (*k*) rates from modeling the MCFT intensities (STAR Methods), we assumed a simple model in which these can increase or decrease with a fixed slope during cell-cycle progression. The

(E) Comparison of the evolution of simulated (top) and obtained (bottom) green and red traces as well as green/red ratios after 48 hr dox-induction of the MCFT-SNAP-PEST and MCFT-SNAP timers in mouse ESCs. Thick line and shades: mean and 95% confidence intervals, respectively.

(F) Percentages of MCFT-tagged proteins for each subcellular localization.

(G) Examples of one MCFT-tagged protein for each subcellular localization (color code refers to F). Images show sfGFP (green, top) and mOrange2 (red, bottom) fluorescence. Scale bars, 20  $\mu$ m.

See also Figure S1 and Table S1.

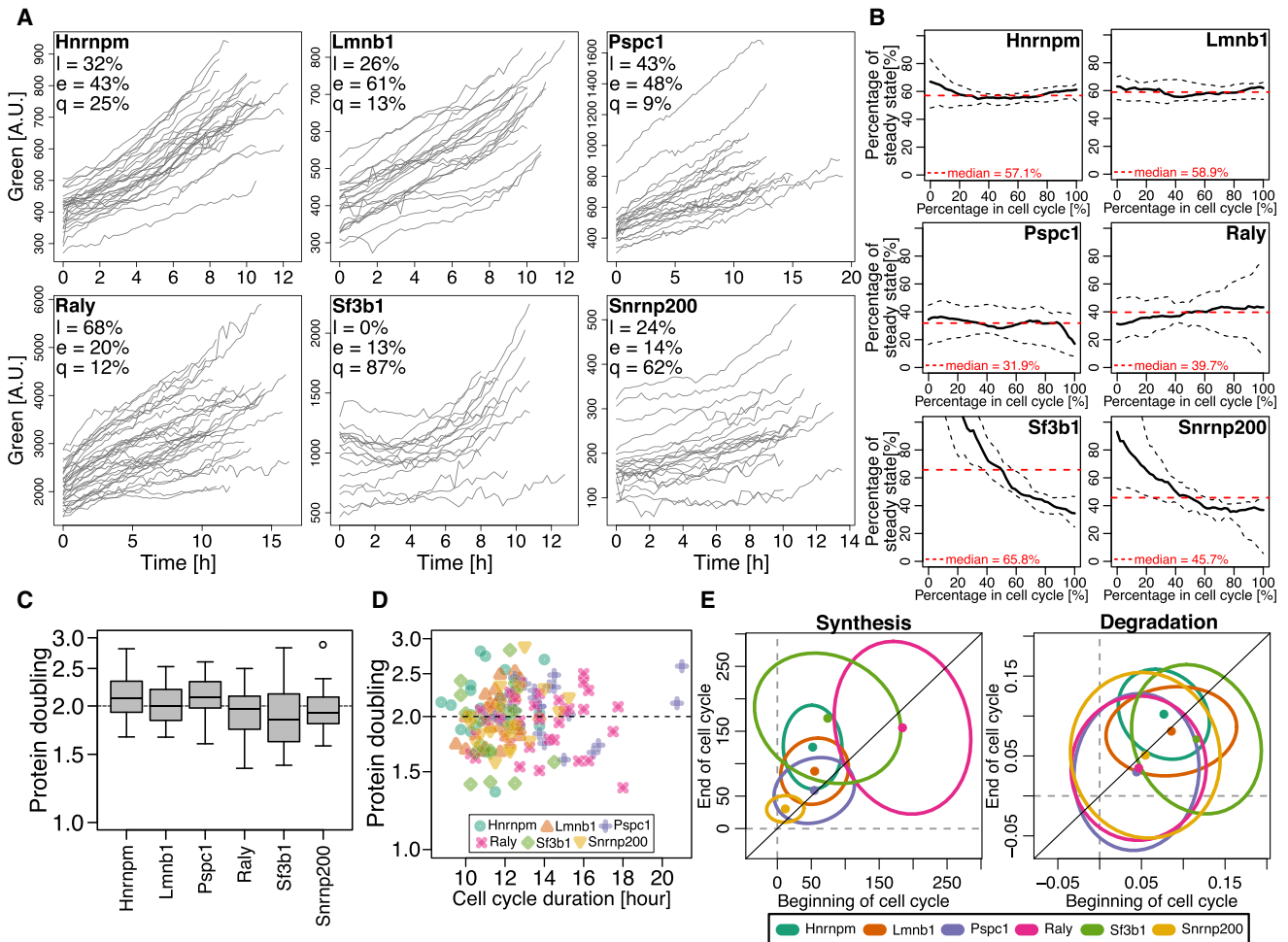


**Figure 2. Protein Accumulation Dynamics during the Cell Cycle**

(A) Single-cell accumulation dynamics of 6 nuclear MCFT-tagged proteins over one cell cycle and percentage of traces best fit by a linear ( $l$ ), exponential ( $e$ ), or quadratic ( $q$ ) model.

(B) Percentage (at any given time) of the steady state ( $s(k)/k(t)$ ) reached by the 6 nuclear MCFT-tagged proteins over the cell cycle. Plain and dashed lines, median and inter-quartile ranges, respectively. Dashed red line, median percentage over the cell cycle.

(C) Protein doubling during the cell cycle for 6 nuclear MCFT-tagged proteins.

(D) Protein doubling as a function of cell-cycle duration for 6 nuclear MCFT-tagged proteins.

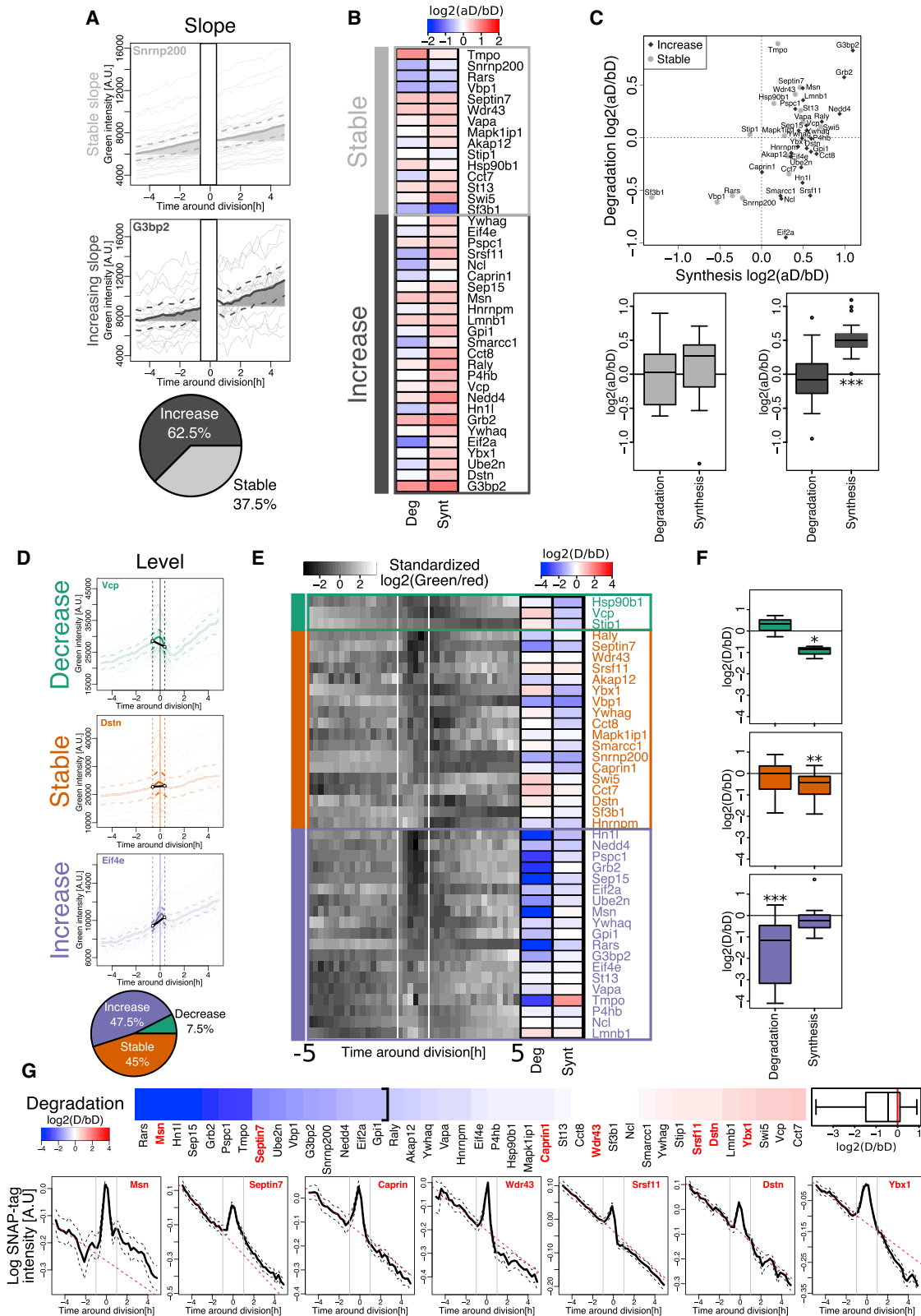
(E) Comparison of synthesis and degradation rates at the beginning and end of the cell cycle for all individual cells of 6 nuclear MCFT-tagged proteins. Mean (dots) and 2D SD (ellipses) of estimated synthesis (left) and degradation (right) rates from all individual cells are shown.

See also [Figure S2](#).

fitted rates showed that the observed sfGFP intensities corresponded to  $\sim 50\%$  of the predicted instantaneous steady state  $s(t)/k(t)$  (Figures 2B and S2A). Furthermore, best fits of the green signals showed that, except for the accumulation of RALY that is better explained by a linear increase, all studied proteins best fit upward bent quadratic or exponential accumulation patterns (Figure 2A). Single-cell protein expression levels at the beginning of the cell cycle did not correlate with a particular protein accumulation dynamics (Figure S2B). Linear and quadratic protein accumulation dynamics have been previously linked to unstable and stable mRNAs, respectively (Cohen et al., 2009).

To quantify the relative increase of protein levels within one cell cycle, we compared green intensities at the end (defined

as the maximum intensity obtained in a window of 1 hr before cytokinesis) and the beginning (defined as the minimal intensity obtained in a window of 1 hr after cytokinesis) of the cell cycle. On average, protein levels in individual cells doubled during each cell cycle (Figure 2C), independently of cell-cycle duration, which varied from 10 to 20 hr (Figure 2D), indicating that the accumulation rate and the cell-cycle duration scale inversely (Figure S2C). As our analysis of the MCFT can also distinguish changes in protein synthesis from changes in protein degradation over the cell cycle, we found that, consistent with a majority of nonlinear accumulation profiles of the green protein (Figure 2A), protein synthesis increased during the cell cycle for 4 out of 6 nuclear proteins,



(legend on next page)

while protein degradation rates did not show clear trends (Figures 2E, S2D, and S2E).

### Protein Accumulation Dynamics around Cell Division

Initial MCFT experiments revealed significant changes in green/red ratios around cytokinesis for several proteins, which motivated us to analyze our full library of 40 MCFT-tagged proteins in a time window ranging from 5 hr before to 5 hr after cytokinesis. Briefly, we tracked green and red fluorescence intensities for 20 cells per clone. Importantly, our tracking approach took into account the integrated fluorescence intensities of the whole cell; thus, our measurements should be fairly insensitive to changes in protein localization during the cell cycle. In contrast to the analysis performed in the previous section, we focused on changes in protein amounts per fixed number of MCFT-tagged alleles (2 tagged alleles in G2) and therefore summed the intensities of the two daughter cells after division. The first time frame where the two daughter cells were separated was defined as  $t = 0$  hr and the individual traces were split in three intervals around cytokinesis: (1) before division (bD) ( $-5$  hr to  $-1$  hr), (2) during division (D) ( $-1$  hr to 30 min), and (3) after division (aD) (30 min to 5 hr). Because these intervals are fairly short on the scale of protein half-lives, we assumed synthesis and degradation rates to be constant in every interval, and estimated best fits of the green and red intensities over the three intervals (STAR Methods; Table S2).

We first focused on changes in protein accumulation rate (slopes) between the aD and bD intervals. While 15 proteins displayed stable accumulation rates, 25 increased their accumulation rate after division (Figures 3A and S3A). We then used the kinetic model to determine how underlying changes in synthesis and degradation explain these profiles. While protein degradation rates were mostly unchanged between the aD and bD intervals, most proteins increasing their accumulation rate in the aD interval displayed a higher synthesis rate per allele after division (Figures 3B and 3C). Therefore, increased protein accumulation rate in G1 phase is mostly due to an increase in protein synthesis per gene copy.

Given that a global decrease in translation and stabilization of subsets of proteins were reported during mitosis (Acebron et al.,

2014; Tanenbaum et al., 2015), we next focused our analysis on a narrower time window centered on cell division. MCFT-tagged proteins were grouped according to their changes in protein levels during a time period of 1 hr before to 30 min after cytokinesis. We found that protein levels either decreased (3/40 clones), were stable (18/40 clones), or increased (19/40 clones) during this time interval (Figures 3D and S3B). Furthermore, a large fraction of proteins displayed a transient decrease in their green/red ratio around division (Figure 3E), suggesting altered protein synthesis and/or degradation around division. We then used our MCFT model to determine how changes in synthesis and degradation rates lead to changes in protein levels in the three groups (Figure 3E; STAR Methods). We found that the decreasing and stable protein profiles seen in the first and second groups are caused by a decrease in protein synthesis during division (Figures 3E and 3F). In contrast, the increasing protein level profiles of the third group were not caused by changes in synthesis rates, but rather by a large decrease in degradation rates (protein stabilization) during division (Figures 3E and 3F). Thus, protein synthesis (Figures 3C and 3F) and degradation (Figure 3F) are modulated differentially and in a protein-specific manner to shape protein accumulation profiles around cytokinesis.

To validate the observed changes in degradation rates using an orthogonal approach, we generated seven dox-inducible cell lines, each expressing the coding sequence of one protein of interest from the MCFT-tagged protein library fused to a C-terminal SNAP-tag. After pulse-labeling with the SiR-647 dye, we measured the decaying signal in a window of 10 hr centered on cytokinesis to estimate how degradation rates change during cell division (Figure 3G). Because the obtained fluorescence intensity values at the time-points around division are imprecise due to cell detachment during cytokinesis, we fitted the SNAP-tag decay signal from 5 to 1 hr before cytokinesis and compared it to the observed decay curve after cytokinesis. For MSN and SEPTIN7, the predicted protein stabilization during division was confirmed by the upward shift in the fluorescence decay curve after cytokinesis (Figure 3G). For CAPRIN1 and WDR43, we observed no major differences in the fluorescence decay traces after cytokinesis as expected from the MCFT data. Lastly,

### Figure 3. Protein Accumulation Dynamics around Division

- (A) Single-cell integrated green fluorescence intensities from  $-5$  hr to  $-1$  hr and  $+0.5$  hr to  $+5$  hr with respect to cytokinesis for representative proteins of each of the two groups (pie chart). Bold lines, population average; dashed lines, 95% confidence intervals.
- (B) Median  $\log_2$  ratio (aD/bD) of degradation and synthesis rates for proteins with either stable or increasing accumulation rate.
- (C) Top:  $\log_2$  (aD/bD) synthesis and degradation rates for all individual proteins. Bottom: distribution of  $\log_2$  (aD/bD) ratios for synthesis and degradation rates of proteins in each of the two groups (\*\* $p < 0.001$ , t test).
- (D) Single-cell integrated green fluorescence intensities from  $-1$  hr to  $+0.5$  hr with respect to cytokinesis for representative proteins of each of the three groups (pie chart). Bold lines, population average; dashed lines, 95% confidence intervals; vertical dashed lines, time points ( $-1$  hr and  $+0.5$  hr) used to estimate changes in green intensity during division; vertical line, cytokinesis.
- (E) Standardized averaged  $\log_2$ (green/red) ratio around division for all 40 proteins. Proteins are first ordered by their group (decrease, stable, or increase) and then ordered by their green/red ratio around cytokinesis. To the right of the heatmap: median  $\log_2$  ratio (D/bD) of the degradation and synthesis rates. White vertical lines,  $-1$  hr and  $+0.5$  hr time points.
- (F) Distribution of  $\log_2$  (D/bD) ratios for synthesis and degradation rates of proteins associated to the decrease, stable, and increase groups (\* $p < 0.05$ , \*\* $p < 0.01$ , and \*\*\* $p < 0.001$ , t test).
- (G) Top: ordered  $\log_2$  ratio of degradation rates during division (D) and before division (bD). The left bracket highlights the proteins with a  $\log_2$  ratio lower than  $-1$ . Bottom: mean SNAP-tag decay (thick black lines) signal and SE (black dashed lines) around division for 7 proteins showing different degradation dynamics around division in the MCFT dataset. Red dashed lines, fitted decays estimated from  $-5$  to  $-1$  hr before division.
- See also Figure S3 and Table S2.

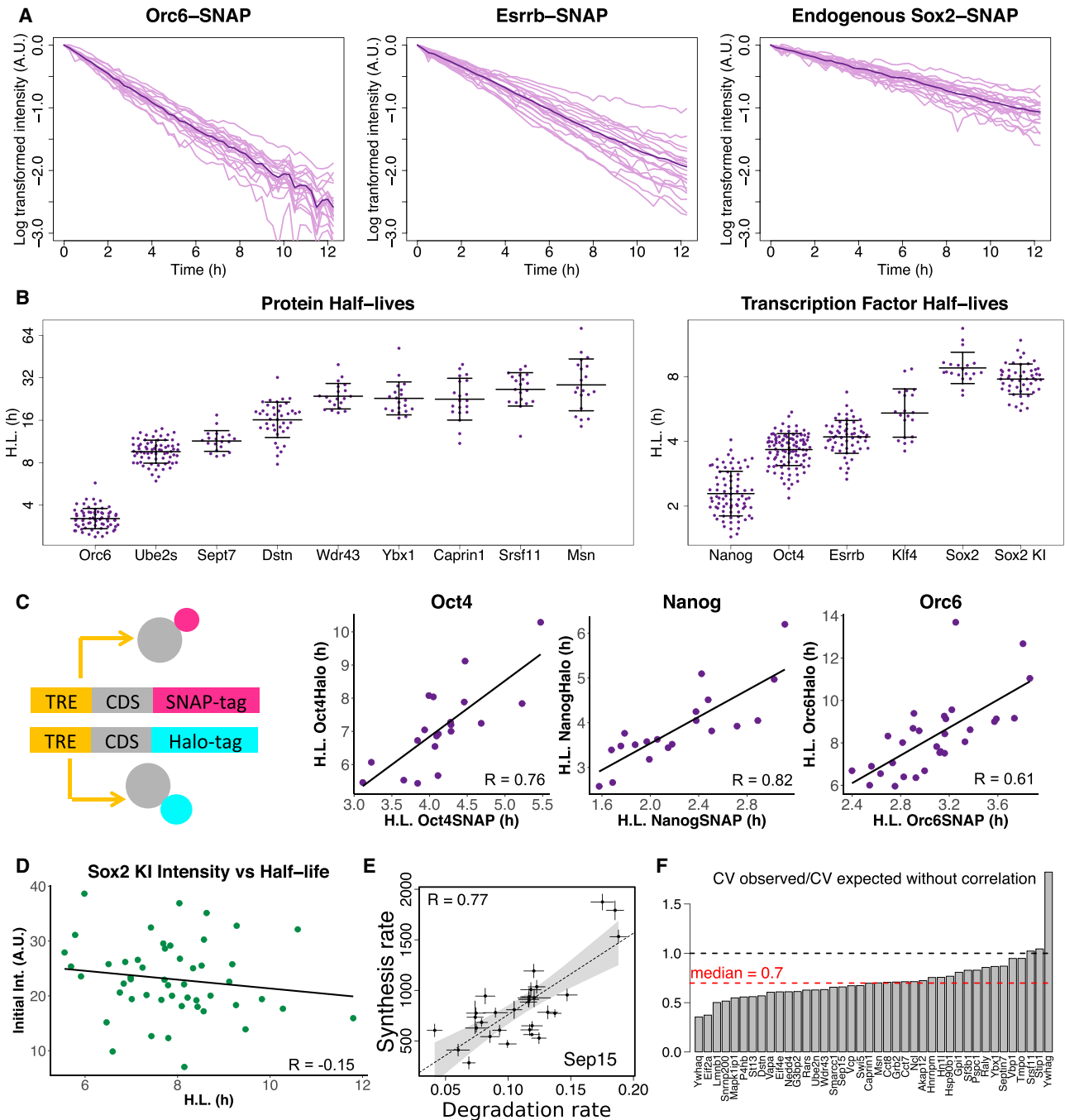


**Figure 4. Protein Degradation Rates Vary Largely between Single Cells**

(A) Examples of log transformed single-cell SNAP-tag fluorescence decays (light purple) and average decay (dark purple) for inducible Orc6-SNAP and Esrrb-SNAP cell lines, and Sox2-SNAP knockin cell line.  $n = 20$  cells each.

(B) Single-cell half-lives (dots), mean and SD (black horizontal lines) of the inducible SNAP-tagged proteins and pluripotency transcription factors and an endogenously tagged SOX2-SNAP.  $n \geq 20$ .

(C) Dual SNAP/Halo-tag imaging of the same tagged protein. Correlations of single-cell half-lives in inducible cell lines in which either OCT4, NANOG, or ORC6 were fused to both a SNAP-tag and a Halo-tag.  $n \geq 20$ .

(D) Correlation between single-cell half-lives and integrated Sox2-SNAP intensities for the Sox2-SNAP knockin cell line.  $n = 50$ .

(legend continued on next page)

for SRSF11, DSTN, and YBX1, we predicted an increase in degradation, which was confirmed by the downward shift in fluorescence decay traces after division, even though the effect was slightly delayed for YBX1. To probe the degradation dynamics around division for shorter-lived proteins, we performed the same experiment with SNAP-tag fusions of five pluripotency-associated transcription factors and observed a decrease in degradation around division for two of them (Figure S3C). We conclude that the SNAP-tag decay data are in very good agreement with the predictions made using the MCFT, confirming that protein degradation rates are altered in a large fraction of proteins around cell division.

### Protein Degradation Rates Vary Significantly between Single Cells

We next aimed at determining how protein degradation rates vary between individual cells. To do so, we used the 12 dox-inducible SNAP-tag fusion cell lines described above and two additional cell lines expressing SNAP-tagged versions of the origin of replication complex member ORC6 and the ubiquitin ligase UBE2S. We determined single-cell protein half-lives in all 14 cell lines by pulse-labeling and fitting of exponential decay curves (Alber and Suter, 2018) (Figures 4A and S1D). Surprisingly, individual cells displayed up to 2- to 3-fold differences between cells with the shortest and longest half-lives and coefficients of variation of 0.2–0.4 (Figures 4B and S4A). Single-cell half-lives were not correlated with the initial integrated SNAP fluorescence intensity (Figures S4B and S4C; Table S3), suggesting that the observed variability is not due to an overexpression artifact. In addition, we measured the half-life of endogenous SOX2 using a knockin cell line in which both SOX2 alleles are endogenously fused to a SNAP-tag (Strebinger et al., 2018) and found similar average SOX2 half-lives and variability as for the corresponding dox-inducible cell line (Figure 4B). To further confirm that the observed cell-to-cell variability in half-lives is not merely due to uncertainty in single-cell measurements and/or exponential fittings, we generated three cell lines in which we expressed both a SNAP-tagged and a Halo-tagged (Los et al., 2008) fusion of the same protein, both under the control of a dox-inducible promoter (Figure 4C). The Halo-tag works on the same principle as the SNAP-tag and it can be labeled with a fluorescent ligand of a different color. If the observed variability in degradation rates stemmed from measurement uncertainty, we would expect the half-lives of the two proteins to be poorly correlated in single cells. We thus determined the half-lives of the SNAP-tagged and the Halo-tagged version of our proteins of interest in single cells. While the Halo-tag prolonged the half-lives of all tagged proteins, the half-lives of the SNAP-tagged and the Halo-tagged proteins were highly correlated in single cells, indicating that the observed variability in protein degradation rates is not due to measurement or exponential fitting uncertainty (Figure 4C; Table S3).

Interestingly, we did not observe higher initial SNAP fluorescence intensity in cells with longer half-lives in the Sox2-SNAP knockin cell line (Figure 4D; Table S3). Because longer protein half-lives should lead to higher protein levels, this suggests that cell-to-cell differences in protein degradation might be compensated at the synthesis level. We thus asked how the synthesis and degradation rates that we previously obtained around division from our 40 MCFT-tagged proteins (Figure 3) correlate in single cells. We observed significant positive correlation between the two rates for most proteins (35/40, 87.5%) in our library (Figures 4E and S4D), suggesting that individual cells compensate for variations in degradation rates by changes in synthesis rates. While a correlation between the two rates is not necessary to preserve the mean protein level (Figure S4E), it is required to buffer protein level fluctuations and allows for maintaining the coefficient of variation to a median level lower than in the absence of correlation between synthesis and degradation rates (Figures 4F and S4F; STAR Methods).

### Cell-to-Cell Variability in Half-Lives Is Caused by Heterogeneity in Global Protein Degradation Rates

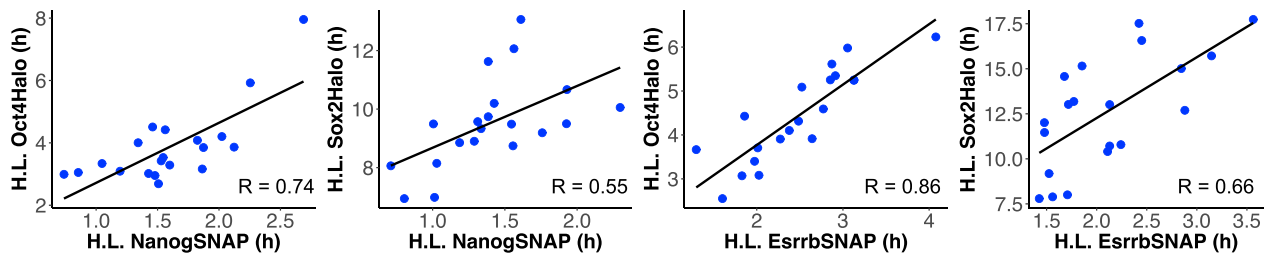
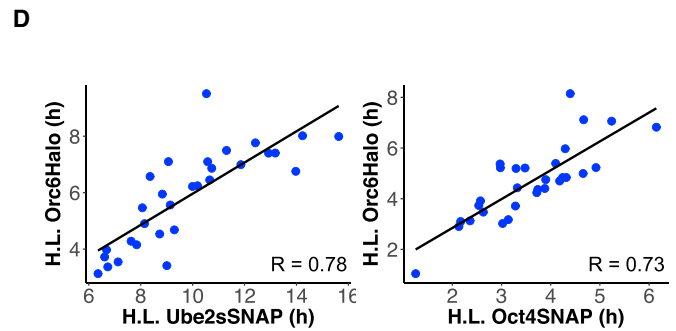
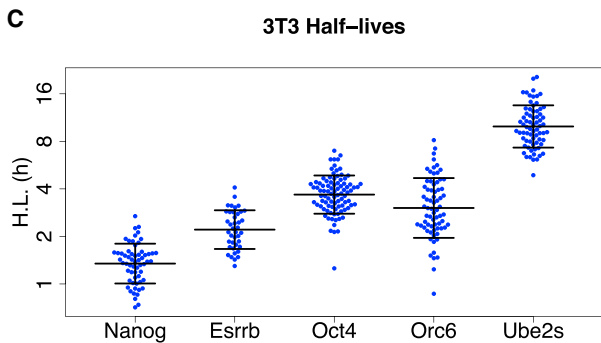
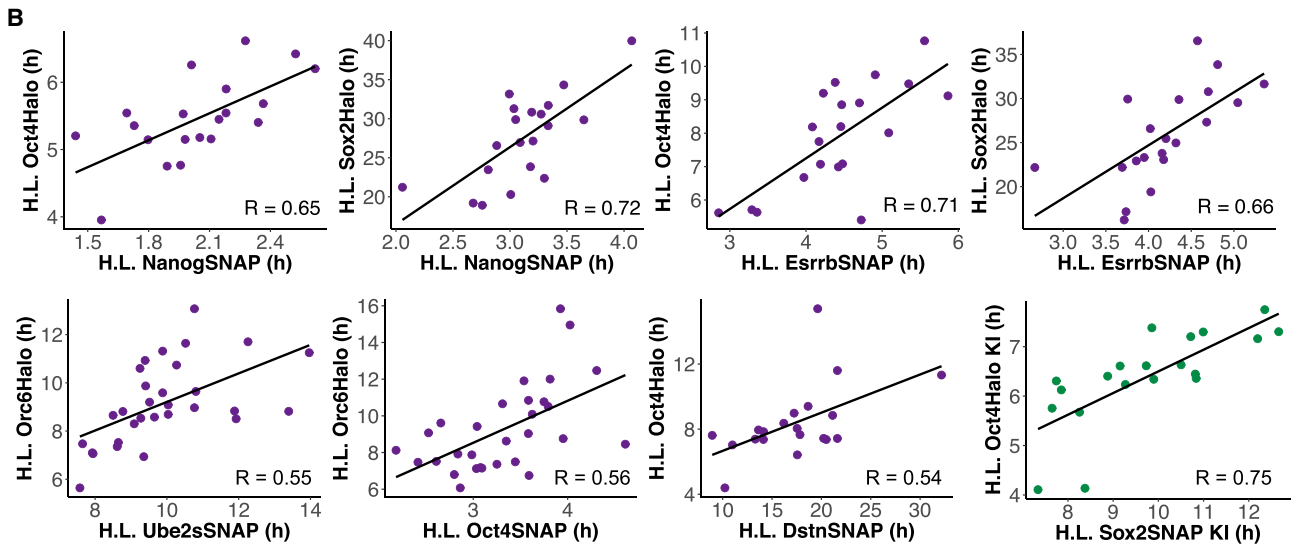
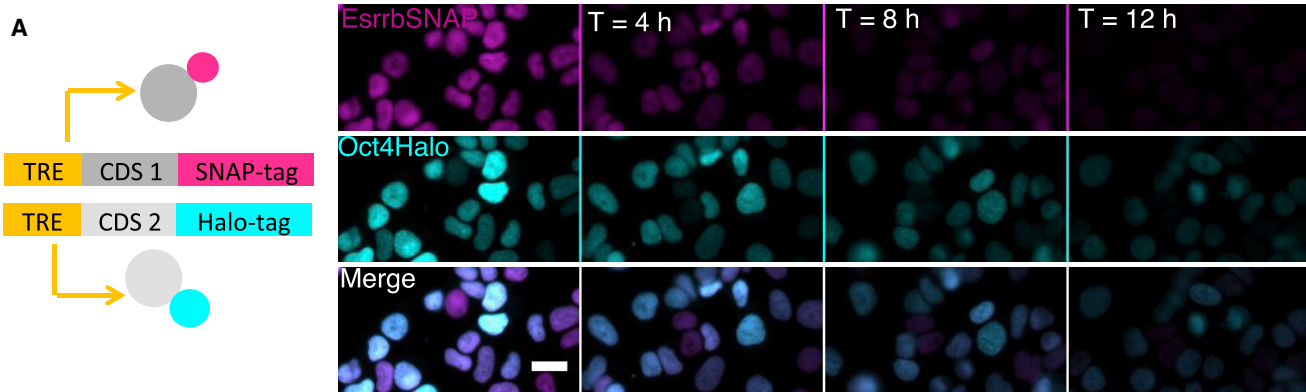
We next asked whether intercellular heterogeneity in protein degradation rates is caused by protein-specific mechanisms or global variability in protein degradation rates. To do so, we generated seven additional dox-inducible ESC lines, in each of which one protein is tagged with a SNAP-tag and another protein is tagged with a Halo-tag, and measured the fluorescence decay from both channels as described above (Figure 5A). Strikingly, the determined half-lives were strongly correlated, not only between functionally related proteins (pluripotency transcription factors), but also between unrelated proteins (Figure 5B; Table S3). Importantly, the fluorescence decay in either channel was not affected by photobleaching (Figure S4G). In addition, we also monitored the SNAP/Halo decay in a SOX2-SNAP/OCT4-Halo knockin cell line (Strebinger et al., 2018) and observed a high correlation of endogenous SOX2 and OCT4 protein half-lives in individual cells (Figure 5B; Table S3). Next, we measured single-cell protein half-lives in NIH 3T3 fibroblasts, and found similar ranges of intercellular variability in protein degradation rates, as well as similar coefficients of variations (Figures 5C and S5A). In addition, we also observed strong correlations in the half-lives of different proteins in single cells (Figures 5D and S5B; Table S3). We conclude that cell-to-cell variability in protein half-lives is largely due to global variations in protein degradation rates in both ESCs and NIH 3T3 fibroblasts.

Finally, we asked whether differences in proteasome activity could account for intercellular variability in protein degradation rates. While the rate-limiting components of protein degradation are not known, raising the levels of ADRM1, which acts as a ubiquitin receptor and is part of the 19S subunit of the proteasome, was reported to increase proteasome activity (Huang and Her, 2017). We thus asked whether the expression levels of ADRM1

(E) Example of correlation between degradation and synthesis rates for the SEP15 protein on  $n = 30$  single cell traces. Lines, SE; dashed line, linear fit; gray area, 95% confidence interval of the linear fit.

(F) Ratio of observed coefficient of variation (CV) versus expected one if synthesis and degradation rates were not correlated for the 40 MCFT-tagged proteins at 50% steady state.

See also Figure S4 and Table S3.



(legend on next page)

or two other putatively non-rate limiting proteasome subunits (proteasome 20S alpha 2 subunit, a component of the proteasome core complex, and TBP7 [PSMC4], an ATPase subunit of the 19S regulatory complex) could explain intercellular heterogeneity in protein half-lives. We first measured the decay of fluorescence from the inducible ORC6-SNAP, UBE2S-SNAP, and OCT4-SNAP cell lines in E14 and NIH 3T3 cells and fixed the cells immediately after time-lapse microscopy. We then stained ADRM1, the proteasome 20S alpha 2, and TBP7 by immunofluorescence and re-imaged the same fields of view from which we measured protein degradation rates. This enabled us to measure protein degradation rates and to quantify the levels of the proteasome subunits of interest within the same cells (Figure 6A). While single-cell half-lives did not correlate with the levels of Proteasome 20S alpha2 and TBP7 (Figures S5C–S5F; Table S3), we found significant negative correlations between ADRM1 levels and protein half-lives for most tested proteins in individual ESCs and NIH 3T3 fibroblasts (Figures 6B and 6C; Table S3). This suggests that heterogeneity in ADRM1 levels contributes to intercellular variability in protein degradation rates. To further investigate the role of ADRM1 expression levels in protein degradation, we generated two cell lines expressing dox-inducible versions of both ADRM1 and SOX2-SNAP or ORC6-SNAP and tested whether ADRM1 overexpression has an impact on protein half-lives (Figure 6D). We observed a moderate decrease in half-lives for both SOX2-SNAP and ORC6-SNAP, suggesting that heterogeneity in expression levels for rate-limiting components of the proteasome contributes to intercellular variability in global protein degradation rates.

## DISCUSSION

Cellular proteins are constantly synthesized and degraded, however, it has been challenging to understand how these two processes interplay to regulate protein levels. Here, we report an approach that allows to disentangle protein synthesis from protein degradation changes in single living cells and in a time-resolved manner. This method should be broadly applicable to any cell type or organism that is amenable to time-lapse fluorescence imaging.

We found major changes in protein synthesis and degradation over the cell cycle, in particular around the time of cell division. Most strikingly, many of our MCFT-tagged proteins were stabilized during division. Whereas a decrease in protein synthesis might be expected, as both transcription and translation are known to decrease substantially during mitosis (Palozola et al., 2017; Tanenbaum et al., 2015), the observed global decrease in protein degradation is surprising. In fact, a similar phenome-

non has only been observed for GSK3 target proteins, which are protected from degradation during M phase (Acebron et al., 2014). However, with the exception of PSPC1, TMPO, and NEDD4, none of the other proteins stabilized during division are known GSK3 targets (Acebron et al., 2014; Taelman et al., 2010). In addition, in our ESC culture conditions, we use inhibitors directly targeting GSK3, thus bypassing the source of cell-cycle-dependent fluctuations in the GSK3 pathway. Therefore, the mechanistic basis of the observed decrease in degradation remains unclear. Mitosis is characterized by massive degradation of cell-cycle-related proteins regulated by two different E3 ligase complexes: the SCF complex, which targets a variety of cell-cycle-associated substrates for degradation at the G2/M transition and the APC/C complex, which regulates the metaphase to anaphase transition by regulating the degradation of CYCLIN A, CYCLIN B, SECURIN, and various other substrates (Shaik et al., 2012). Therefore, this could potentially limit protein degradation resources for other cellular proteins. However, further studies will be required to explore this hypothesis. The consequences of protein stabilization around cell division for cellular physiology are also unclear. In the case of GSK3 target genes, blocking Wnt-dependent protection from degradation during mitosis has been shown to significantly reduce the cell size of daughter cells (Acebron et al., 2014). Because the stabilization of proteins we describe here affects a large fraction of proteins, it may also contribute to maintaining protein levels and thereby cell size in newly born cells.

The compensation of intercellular variability of degradation rates by corresponding changes in synthesis rates suggests a coupling between these two processes. Interestingly, mammalian target of rapamycin complex 1 (mTORC1) activity was shown to regulate both protein synthesis and degradation by increasing the synthesis of both ribosomal and proteasomal components and by facilitating the formation of the immunoproteasome (Yun et al., 2016; Zhang et al., 2014). Further studies shall clarify whether intercellular variability in mTORC1 activity underlies coordinated intercellular variability in protein synthesis and degradation rates.

While gene expression levels displays large intercellular variability within isogenic and phenotypically homogeneous populations in a broad range of organisms (Kaern et al., 2005; Raj and van Oudenaarden, 2008), the contribution of variability in protein degradation rates remains largely uncharacterized. Here, we found that these display up to 2- to 3-fold variability within ESC and fibroblast cell populations and are at least partly due to heterogeneous expression levels of a rate-limiting component of the proteasome. The heterogeneity in protein degradation rates we describe acts as a global source of extrinsic noise that seemingly

### Figure 5. Cell-to-Cell Variability in Protein Half-Lives Is Caused by Global Differences in Protein Degradation Rates in ESCs and NIH 3T3 Fibroblasts

(A) Dual SNAP/Halo-tag imaging of 2 different tagged proteins. Construct scheme and images showing the fluorescence decay of the inducible Esrrb-SNAP/Oct4-Halo cell line. Scale bar, 20  $\mu$ m.

(B) Single-cell half-life correlations for 7 combinations of SNAP- and Halo-tagged inducible proteins and a Sox2-SNAP Oct4-Halo knockin (KI) cell line.  $n \geq 20$  each.

(C) Single-cell half-lives (dots), mean, and SD (black horizontal lines), for the inducible SNAP-tag fusion proteins in NIH 3T3 cells.  $n \geq 20$  each.

(D) Single-cell half-life correlations for 6 combinations of SNAP- and Halo-tagged proteins in NIH 3T3 cells.  $n \geq 20$  each.

See also Figure S5 and Table S3.

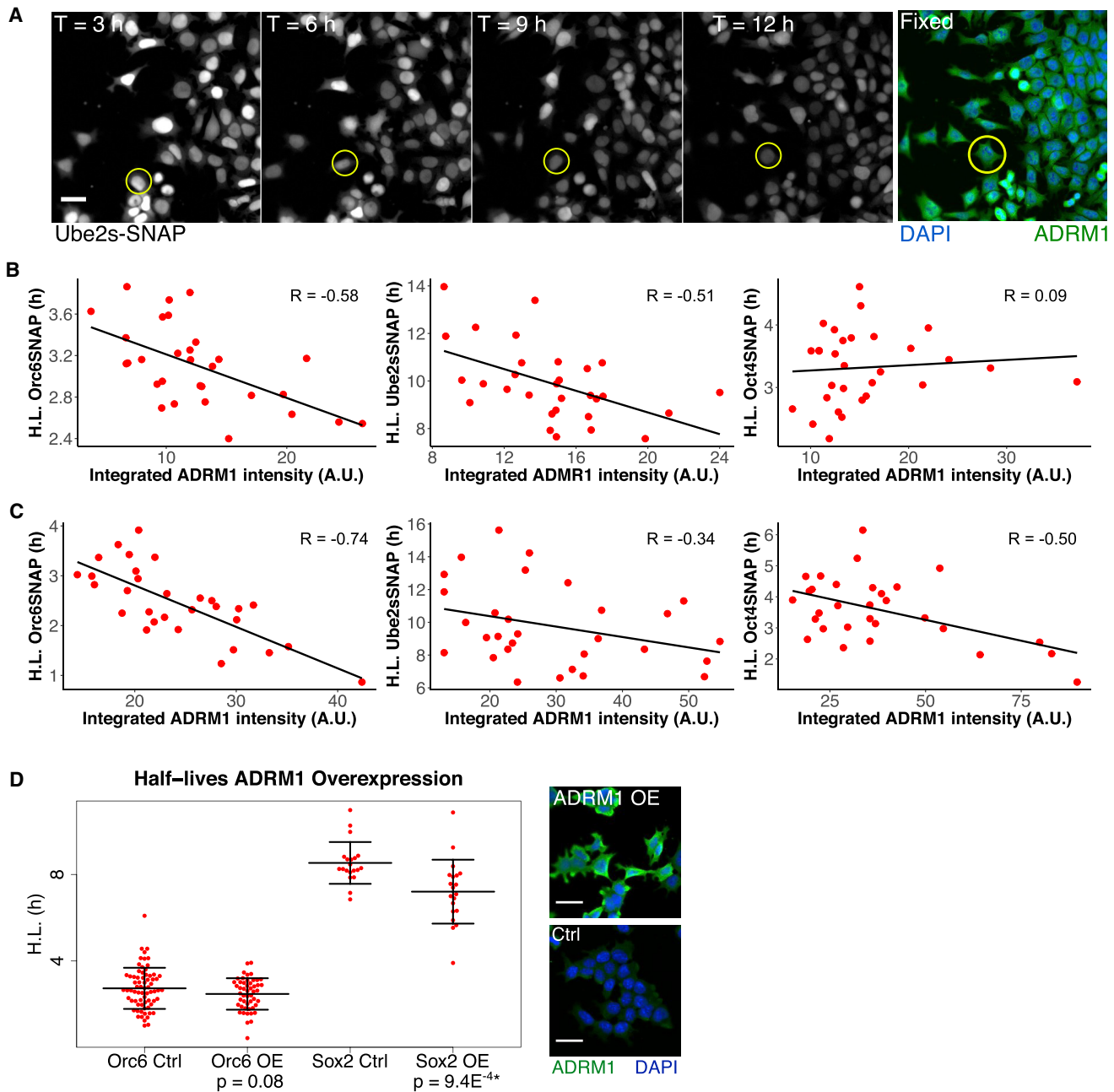


**Figure 6. Variability in Proteasome Activity Contributes to Intercellular Heterogeneity in Protein Half-Lives**

(A) Decay of fluorescence in the E14 Ube2s-SNAP cell line and an ADRM1 immunofluorescence (IF) image of the same x/y-coordinates. One representative cell is highlighted to illustrate single-cell time-lapse monitoring followed by IF quantification of ADRM1. Scale bar, 30  $\mu$ m.

(B) Correlations of single-cell protein half-lives and ADRM1 expression levels in the E14 Orc6-SNAP, Ube2s-SNAP, and Oct4-SNAP cell lines. n = 30.

(C) Correlations of single-cell protein half-lives and ADRM1 expression levels in the NIH 3T3 Orc6-SNAP, Ube2s-SNAP, and Oct4-SNAP cell lines. n = 30.

(D) Single-cell protein half-lives (dots), mean, and SD (black horizontal lines) of ORC6-SNAP and SOX2-SNAP upon 24 hr of ADRM1 overexpression (500 ng/mL dox) as compared to data shown in Figure 4B. Representative immunofluorescence images of ADRM1 overexpression cells versus cells with endogenous ADRM1 levels are shown. Scale bar, 30  $\mu$ m.

See also Figure S5 and Table S3.

affects all targets of the ubiquitin proteasome system to a similar extent. This contrasts with other sources of gene expression noise such as transcription, which is largely gene-specific (Suter

et al., 2011). Whether protein degradation rate variability affects proteome levels proportionally and thereby alters cell size or growth shall be clarified by further studies.

## STAR★METHODS

Detailed methods are provided in the online version of this paper and include the following:

- **KEY RESOURCES TABLE**
- **CONTACT FOR REAGENT AND RESOURCE SHARING**
- **EXPERIMENTAL MODEL AND SUBJECT DETAILS**
  - Cell lines and culture
- **METHOD DETAILS**
  - Plasmid construction
  - Production of lentiviral vectors and generation of stable cell lines
  - Identification of insertion sites by 3' Rapid Amplification of cDNA Ends
  - Time-lapse fluorescence microscopy
  - Image processing and analysis
  - Immunofluorescence experiments
  - Modeling the mammalian cell-optimized tandem fluorescent timer (MCFT)
  - Estimating the fluorescence correction factor  $\alpha$
  - Estimating the sfGFP maturation time
  - Estimating the mOrange2 maturation time
  - Quantification of FRET effects in the MCFT
  - Fitting the MCFT during interphase
  - Validating synthesis and degradation retrieval during interphase
  - Fitting the MCFT around cell division
  - Validating synthesis and degradation retrieval around cell division
  - Analysis of correlations in synthesis and degradation rates
- **QUANTIFICATION AND STATISTICAL ANALYSIS**
- **DATA AND SOFTWARE AVAILABILITY**

## SUPPLEMENTAL INFORMATION

Supplemental Information includes six figures and three tables and can be found with this article online at <https://doi.org/10.1016/j.molcel.2018.07.023>.

## ACKNOWLEDGMENTS

We thank Cédric Deluz, Ricardo Camilo Moreira, and Nattapong Sanguankiatichai for help with cell line generation; Aleksandra Mandic for help with image analysis; Fabien Kuttler from the Swiss Federal Institute of Technology (EPFL) Biomolecular Screening Facility (EPFL-BSF) and Luigi Bozzo and José Artacho from the EPFL Bioimaging and Optics Core Facility (EPFL-BIOP) for assistance in imaging; and Nicholas Phillips for reading and commenting on the manuscript. Fluorescence-activated cell sorting was performed in the EPFL Flow Cytometry Core Facility (EPFL-FCCF). This work was supported by a Canadian Institute of Health Research (CIHR 358808 to E.R.P.) and SystemsX.ch transition postdoc fellowships (51FSP0163584 to E.R.P.), the Pierre Mercier Foundation (to D.M.S.), and the Teofilo Rossi di Montelera e di Premuda Foundation and an anonymous donor, both advised by CARIGEST SA (to D.M.S.).

## AUTHOR CONTRIBUTIONS

Conceptualization, A.B.A. and D.M.S.; Methodology, A.B.A., D.M.S., E.R.P., and F.N.; Software, E.R.P.; Formal Analysis, A.B.A. and E.R.P.; Investigation, A.B.A., E.R.P., and M.B.; Resources, D.M.S. and F.N.; Writing – Original Draft, A.B.A., E.R.P., and D.M.S.; Writing – Review & Editing, A.B.A., E.R.P., D.M.S.,

and F.N.; Funding Acquisition, E.R.P., D.M.S., and F.N.; Supervision, D.M.S. and F.N.

## DECLARATION OF INTERESTS

The authors declare no competing interests.

Received: April 4, 2018

Revised: June 5, 2018

Accepted: July 20, 2018

Published: August 23, 2018

## REFERENCES

- Acebron, S.P., Karaulanov, E., Berger, B.S., Huang, Y.-L., and Niehrs, C. (2014). Mitotic wnt signaling promotes protein stabilization and regulates cell size. *Mol. Cell* *54*, 663–674.
- Alber, A.B., and Suter, D.M. (2018). Single-cell quantification of protein degradation rates by time-lapse fluorescence microscopy in adherent cell culture. *J. Vis. Exp.* (132) <https://doi.org/10.3791/56604>.
- Aviner, R., Geiger, T., and Elroy-Stein, O. (2013). Novel proteomic approach (PUNCH-P) reveals cell cycle-specific fluctuations in mRNA translation. *Genes Dev.* *27*, 1834–1844.
- Balleza, E., Kim, J.M., and Cluzel, P. (2018). Systematic characterization of maturation time of fluorescent proteins in living cells. *Nat. Methods* *15*, 47–51.
- Barry, J.D., Donà, E., Gilmour, D., and Huber, W. (2016). TimerQuant: a modeling approach to tandem fluorescent timer design and data interpretation for measuring protein turnover in embryos. *Development* *143*, 174–179.
- Bieler, J., Cannavo, R., Gustafson, K., Gobet, C., Gattfield, D., and Naef, F. (2014). Robust synchronization of coupled circadian and cell cycle oscillators in single mammalian cells. *Mol. Syst. Biol.* *10*, 739.
- Bojkowska, K., Santoni de Sio, F., Barde, I., Offner, S., Verp, S., Heinis, C., Johnsson, K., and Trono, D. (2011). Measuring in vivo protein half-life. *Chem. Biol.* *18*, 805–815.
- Chang, H.H., Hemberg, M., Barahona, M., Ingber, D.E., and Huang, S. (2008). Transcriptome-wide noise controls lineage choice in mammalian progenitor cells. *Nature* *453*, 544–547.
- Cohen, A.A., Geva-Zatorsky, N., Eden, E., Frenkel-Morgenstern, M., Issaeva, I., Sigal, A., Milo, R., Cohen-Saidon, C., Liron, Y., Kam, Z., et al. (2008). Dynamic proteomics of individual cancer cells in response to a drug. *Science* *322*, 1511–1516.
- Cohen, A.A., Kalisky, T., Mayo, A., Geva-Zatorsky, N., Danon, T., Issaeva, I., Kopito, R.B., Perzov, N., Milo, R., Sigal, A., and Alon, U. (2009). Protein dynamics in individual human cells: experiment and theory. *PLoS ONE* *4*, e4901.
- Coldwell, M.J., Cowan, J.L., Vlasak, M., Mead, A., Willett, M., Perry, L.S., and Morley, S.J. (2013). Phosphorylation of eIF4GII and 4E-BP1 in response to nocodazole treatment: a reappraisal of translation initiation during mitosis. *Cell Cycle* *12*, 3615–3628.
- Deluz, C., Friman, E.T., Strebinger, D., Benke, A., Raccaud, M., Callegari, A., Leleu, M., Manley, S., and Suter, D.M. (2016). A role for mitotic bookmarking of SOX2 in pluripotency and differentiation. *Genes Dev.* *30*, 2538–2550.
- Harikumar, A., Edupuganti, R.R., Sorek, M., Azad, G.K., Markoulaki, S., Sehnalová, P., Legartová, S., Bártová, E., Farkash-Amar, S., Jaenisch, R., et al. (2017). An endogenously tagged fluorescent fusion protein library in mouse embryonic stem cells. *Stem Cell Reports* *9*, 1304–1314.
- Huang, Z.-N., and Her, L.-S. (2017). The ubiquitin receptor ADRM1 modulates HAP40-induced proteasome activity. *Mol. Neurobiol.* *54*, 7382–7400.
- Jarvik, J.W., Adler, S.A., Telmer, C.A., Subramaniam, V., and Lopez, A.J. (1996). CD-tagging: a new approach to gene and protein discovery and analysis. *Biotechniques* *20*, 896–904.
- Kaern, M., Elston, T.C., Blake, W.J., and Collins, J.J. (2005). Stochasticity in gene expression: from theories to phenotypes. *Nat. Rev. Genet.* *6*, 451–464.

- Keppeler, A., Gendreizig, S., Gronemeyer, T., Pick, H., Vogel, H., and Johnsson, K. (2003). A general method for the covalent labeling of fusion proteins with small molecules in vivo. *Nat. Biotechnol.* *21*, 86–89.
- Khmelniskii, A., Keller, P.J., Bartosik, A., Meurer, M., Barry, J.D., Mardin, B.R., Kaufmann, A., Trautmann, S., Wachsmuth, M., Pereira, G., et al. (2012). Tandem fluorescent protein timers for in vivo analysis of protein dynamics. *Nat. Biotechnol.* *30*, 708–714.
- Khmelniskii, A., Blaszczyk, E., Pantazopoulou, M., Fischer, B., Omnus, D.J., Le Dez, G., Brossard, A., Gunnarsson, A., Barry, J.D., Meurer, M., et al. (2014). Protein quality control at the inner nuclear membrane. *Nature* *516*, 410–413.
- Khmelniskii, A., Meurer, M., Ho, C.-T., Besenbeck, B., Füller, J., Lemberg, M.K., Bukau, B., Mogk, A., and Knop, M. (2016). Incomplete proteasomal degradation of green fluorescent proteins in the context of tandem fluorescent protein timers. *Mol. Biol. Cell* *27*, 360–370.
- Kolb, V.A., Makeyev, E.V., and Spirin, A.S. (1994). Folding of firefly luciferase during translation in a cell-free system. *EMBO J.* *13*, 3631–3637.
- Los, G.V., Encell, L.P., McDougall, M.G., Hartzell, D.D., Karassina, N., Zimprich, C., Wood, M.G., Learish, R., Ohana, R.F., Urh, M., et al. (2008). HaloTag: a novel protein labeling technology for cell imaging and protein analysis. *ACS Chem. Biol.* *3*, 373–382.
- Molina, N., Suter, D.M., Cannavo, R., Zoller, B., Gotic, I., and Naef, F. (2013). Stimulus-induced modulation of transcriptional bursting in a single mammalian gene. *Proc. Natl. Acad. Sci. USA* *110*, 20563–20568.
- Palozola, K.C., Donahue, G., Liu, H., Grant, G.R., Becker, J.S., Cote, A., Yu, H., Raj, A., and Zaret, K.S. (2017). Mitotic transcription and waves of gene reactivation during mitotic exit. *Science* *358*, 119–122.
- Parsons, G.G., and Spencer, C.A. (1997). Mitotic repression of RNA polymerase II transcription is accompanied by release of transcription elongation complexes. *Mol. Cell. Biol.* *17*, 5791–5802.
- Raj, A., and van Oudenaarden, A. (2008). Nature, nurture, or chance: stochastic gene expression and its consequences. *Cell* *135*, 216–226.
- Rogers, S., Wells, R., and Rechsteiner, M. (1986). Amino acid sequences common to rapidly degraded proteins: the PEST hypothesis. *Science* *234*, 364–368.
- Schindelin, J., Arganda-Carreras, I., Frise, E., Kaynig, V., Longair, M., Pietzsch, T., Preibisch, S., Rueden, C., Saalfeld, S., Schmid, B., et al. (2012). Fiji: an open-source platform for biological-image analysis. *Nat. Methods* *9*, 676–682.
- Shaik, S., Fukushima, H., Wang, Z., and Wei, W. (2012). Protein Degradation in Cell Cycle. In *eLS* (John Wiley & Sons). <https://doi.org/10.1002/9780470015902.a0023158>.
- Shaner, N.C., Lin, M.Z., McKeown, M.R., Steinbach, P.A., Hazelwood, K.L., Davidson, M.W., and Tsien, R.Y. (2008). Improving the photostability of bright monomeric orange and red fluorescent proteins. *Nat. Methods* *5*, 545–551.
- Sigal, A., Danon, T., Cohen, A., Milo, R., Geva-Zatorsky, N., Lustig, G., Liron, Y., Alon, U., and Perzov, N. (2007). Generation of a fluorescently labeled endogenous protein library in living human cells. *Nat. Protoc.* *2*, 1515–1527.
- Strebinger, D., Friman, E.T., Deluz, C., Govindan, S., Alber, A.B., and Suter, D.M. (2018). Endogenous fluctuations of OCT4 and SOX2 bias pluripotent cell fate decisions. *bioRxiv*. <https://doi.org/10.1101/299073>.
- Stumpf, C.R., Moreno, M.V., Olshen, A.B., Taylor, B.S., and Ruggero, D. (2013). The translational landscape of the mammalian cell cycle. *Mol. Cell* *52*, 574–582.
- Suter, D.M., Cartier, L., Bettiol, E., Tirefort, D., Jaconi, M.E., Dubois-Dauphin, M., and Krause, K.-H. (2006). Rapid generation of stable transgenic embryonic stem cell lines using modular lentivectors. *Stem Cells* *24*, 615–623.
- Suter, D.M., Molina, N., Gatfield, D., Schneider, K., Schibler, U., and Naef, F. (2011). Mammalian genes are transcribed with widely different bursting kinetics. *Science* *332*, 472–474.
- Taelman, V.F., Dobrowolski, R., Plouhinec, J.-L., Fuentealba, L.C., Vorwald, P.P., Gumper, I., Sabatini, D.D., and De Robertis, E.M. (2010). Wnt signaling requires sequestration of glycogen synthase kinase 3 inside multivesicular endosomes. *Cell* *143*, 1136–1148.
- Tanenbaum, M.E., Stern-Ginossar, N., Weissman, J.S., and Vale, R.D. (2015). Regulation of mRNA translation during mitosis. *eLife* *4*, e07957.
- Yeku, O., and Frohman, M.A. (2011). Rapid amplification of cDNA ends (RACE). *Methods Mol. Biol.* *703*, 107–122.
- Yun, Y.S., Kim, K.H., Tschida, B., Sachs, Z., Noble-Orcutt, K.E., Moriarity, B.S., Ai, T., Ding, R., Williams, J., Chen, L., et al. (2016). mTORC1 coordinates protein synthesis and immunoproteasome formation via PRAS40 to prevent accumulation of protein stress. *Mol. Cell* *61*, 625–639.
- Zhang, Y., Nicholatos, J., Dreier, J.R., Ricoult, S.J.H., Widenmaier, S.B., Hotamisligil, G.S., Kwiatkowski, D.J., and Manning, B.D. (2014). Coordinated regulation of protein synthesis and degradation by mTORC1. *Nature* *513*, 440–443.

## STAR★METHODS

### KEY RESOURCES TABLE

REAGENT or RESOURCE	SOURCE	IDENTIFIER
<b>Antibodies</b>		
ADRM1 antibody (C-7)	Santa Cruz Biotechnology	Cat# sc-376221; RRID: AB_10991330
Anti-Tbp7 antibody [EPR9911(B)]	Abcam	Cat# ab139184
Anti-Proteasome 20S alpha 2 antibody [EPR5453]	Abcam	Cat# ab109525; RRID: AB_10865271
<b>Chemicals, Peptides, and Recombinant Proteins</b>		
Glasgow Minimum Essential Medium	Sigma-Aldrich	Cat# G5154
Dulbecco's Modified Eagle Medium, high glucose, pyruvate	ThermoFisher	Cat# 41966029
Fetal Bovine Serum, embryonic stem cell-qualified	ThermoFisher	Cat# 16141079
Fetal Bovine Serum	ThermoFisher	Cat#10270106
Sodium pyruvate solution	Sigma-Aldrich	Cat# 113-24-6
Penicillin-Streptomycin	BioConcept	Cat# 4-01F00H
L-Glutamine 200mM	ThermoFisher	Cat# 25030-024
2-Mercaptoethanol	Sigma-Aldrich	Cat# 63689-25ML-F
Leukemia Inhibitory factor	Home made	N/A
GSK-3 Inhibitor XVI	Merck Millipore	Cat# 361559
Trypsin-EDTA-Solution	Sigma-Aldrich	Cat# T4049
Recombinant Mouse E-Cadherin Fc Chimera protein	R&D systems	Cat# 748-EC-050
Recombinant Rat E-Cadherin Fc Chimera Protein	R&D systems	Cat# 8144-EC-050
FluoroBrite DMEM	ThermoFisher	Cat# A18967-01
Doxycycline hyclate	Sigma-Aldrich	Cat# D9891
SNAP-Cell® 647-SiR	New England BioLabs	Cat# S9102S
HaloTag® TMR Ligand	Promega	Cat# G8251
<b>Critical Commercial Assays</b>		
GenElute Mammalian Total RNA Miniprep Kit	Sigma	Cat# RTN70-1KT
In-Fusion® HD Cloning Plus	Clontech	Cat# 638911
SuperScript II Reverse Transcriptase	Invitrogen	Cat# 18064-014
<b>Deposited Data</b>		
Imaging dataset	Mendeley Data	<a href="https://data.mendeley.com/datasets/sgyzkr223j/1">https://data.mendeley.com/datasets/sgyzkr223j/1</a>
<b>Experimental Models: Cell Lines</b>		
E14 embryonic stem cell line	Didier Trono, EPFL	N/A
NIH 3T3 cell line	Ueli Schibler, University of Geneva	N/A
<b>Oligonucleotides</b>		
cDNA synthesis primer: 5'GCTCGCGAGCGCGTTTAAACGCGCACGCGTTTTTTTTTTT TTTTTTTTVN3'	This paper	N/A
1 <sup>st</sup> RACE primer fw: 5'AGCTCGCCGATCACTATCAACAGAA3'	This paper	N/A
1 <sup>st</sup> RACE primer rv: 5' GCTCGCGAGCGCGTTTAAAC3'	This paper	N/A
2 <sup>nd</sup> RACE primer fw: 5'CGACAACCACTACCTGAGTACCCAGAC3'	This paper	N/A
2 <sup>nd</sup> RACE primer rv: 5'GCGTTTAAACGCGCACGCGT3'	This paper	N/A
<b>Recombinant DNA</b>		
pLVTRE3GMCS	<a href="#">Deluz et al., 2016</a> (David Suter Lab)	N/A
pLVTRE3GMCS-Sox2-YPET	<a href="#">Deluz et al., 2016</a> (David Suter Lab)	N/A

(Continued on next page)

**Continued**

REAGENT or RESOURCE	SOURCE	IDENTIFIER
pLV-pGK-rtTA3G-IRES-Bsd	<a href="#">Deluz et al., 2016</a> (David Suter Lab)	N/A
pSTAR	Ka Yi Hui, University of Geneva	N/A
pLVTRE3G-MCFT-SNAP-NLS	This paper	N/A
pLVTRE3G-MCFT-SNAP-NLS-NLS-PEST	This paper	N/A
pSTAR-SA-mOrange2-sfGFP-SD	This paper	N/A
pLVTRE3G-Sept7-SNAP	This paper	N/A
pLVTRE3G-Wdr43-SNAP	This paper	N/A
pLVTRE3G-Dstn-SNAP	This paper	N/A
pLVTRE3G-Msn-SNAP	This paper	N/A
pLVTRE3G-Caprin1-SNAP	This paper	N/A
pLVTRE3G-Srsf11-SNAP	This paper	N/A
pLVTRE3G-Ybx1-SNAP	This paper	N/A
pLVTRE3G-Orc6-SNAP	This paper	N/A
pLVTRE3G-Ube2S-SNAP	This paper	N/A
pLVTRE3G-Sox2-SNAP	This paper	N/A
pLVTRE3G-Oct4-SNAP	This paper	N/A
pLVTRE3G-Nanog-SNAP	This paper	N/A
pLVTRE3G-Esrrb-SNAP	This paper	N/A
pLVTRE3G-Klf4-SNAP	This paper	N/A
pLVTRE3G-Klf4-SNAP	This paper	N/A
pLVTRE3G-Sox2-Halo	This paper	N/A
pLVTRE3G-Oct4-Halo	This paper	N/A
pLVTRE3G-Nanog-Halo	This paper	N/A
pLVTRE3G-Orc6-Halo	This paper	N/A
pLVTRE3G-mCherry-sfGFP-SNAP-NLS	This paper	N/A
pLVTRE3G-sfGFP-SNAP-NLS-NLS	This paper	N/A
pLVTRE3G-sfGFP-FLUC-NLS-PEST	This paper	N/A
pCMV6-Entry-Adrm1	OriGene	Cat# MR206404
pLVTRE3G-Adrm1	This paper	N/A
<b>Software and Algorithms</b>		
MATLAB R2014a	Mathworks	N/A
R	R Core Team	<a href="https://www.r-project.org/">https://www.r-project.org/</a>
FIJI	N/A	<a href="http://imagej.net/Fiji">http://imagej.net/Fiji</a>

**CONTACT FOR REAGENT AND RESOURCE SHARING**

Further information and requests for resources and reagents should be directed to and will be fulfilled by the Lead Contact, David Suter ([david.suter@epfl.ch](mailto:david.suter@epfl.ch)).

**EXPERIMENTAL MODEL AND SUBJECT DETAILS**

**Cell lines and culture**

The E14 ES cell line (provided by Didier Trono, EPFL) was used for all ES cell experiments. Cells were routinely cultured at 37°C and 5% CO<sub>2</sub> in GMEM (Sigma, G5154), supplemented with 10% ES cell-qualified fetal bovine serum (Thermofisher, 16141-079), 2 mM sodium pyruvate (Sigma-Aldrich, 113-24-6), 1% non-essential amino acids (Thermofisher, 11140-035), 1% penicillin/streptomycin (BioConcept, 4-01F00H), 2 mM L-glutamine (Thermofisher, 25030-024), 100 μM 2-mercaptoethanol (Sigma-Aldrich, 63689-25ML-F), leukemia inhibitory factor (concentration not determined, produced in the lab by transient transfection of HEK293T cells and tested for its potential to maintain pluripotency), 3 μM GSK-3 Inhibitor XVI (Merck Millipore, 361559) and 0.8 μM PD184352 (Sigma-Aldrich, 391210-10-9). Cells were grown on 100 mm cell culture dishes or 6-well plates coated with 0.1% gelatin up to confluences of 70% and split 1/10 every 2-3 days upon trypsinization.

NIH 3T3 cells (provided by Ueli Schibler, University of Geneva) and HEK293T cells (ATCC) were routinely cultured at 37°C and 5% CO<sub>2</sub> in DMEM (Thermofisher; 41966029), supplemented with 10% fetal bovine serum (Thermofisher, 10270106) and 1% penicillin/streptomycin (BioConcept, 4-01F00H). Cells were grown in 100 mm cell culture dishes or 6-well plates up to a confluence of 70% and split 1/6 every 2-3 days.

## METHOD DETAILS

### Plasmid construction

The inducible MCFT-SNAP and MCFT-SNAP-PEST constructs were generated using the pLVTR3GMCS lentiviral vector (Deluz et al., 2016) as follows: First, the mOrange2-AgeI-sfGFP sequence was PCR-amplified using primers with overhangs encoding Sall and EcoRV restriction sites and ligated into the pLVTR3GMCS vector. To generate a short-lived inducible MCFT, the NLS-PEST sequence was PCR amplified from the pSTAR vector (gift from Ka Yi Hui, University of Geneva) with overhangs containing a 5' and a 3' homology arm and inserted into the inducible mOrange2-sfGFP vector by infusion cloning (Clontech) upon EcoRV digestion of the vector. Finally, the SNAP-tag sequence was PCR-amplified using overhangs encoding 5' and 3' homology arms and an NLS sequence on the 3' end and inserted into the short-lived and long-lived MCFT vectors by infusion cloning upon digest of the vectors with EcoRV. This led to the generation of the final pLVTR3G-mOrange2-sfGFP-SNAP-NLS-NLS-PEST (further referred to as inducible MCFT-SNAP-PEST) and pLVTR3G-mOrange2-sfGFP-SNAP-NLS (further referred to as inducible MCFT-SNAP) vectors.

For the generation of the endogenous CD-tagged MCFT clones, a pSTAR-SA-mOrange2-sfGFP-SD vector was produced. First, the mOrange2-AgeI-sfGFP sequence was PCR-amplified using overhangs containing the sequences for a splice acceptor (SA) and a splice donor (SD) as well as restriction sites for ClaI and NheI. The PCR product was then digested with ClaI and NheI and ligated into the pSTAR vector (gift from Ka Yi Hui, University of Geneva).

For the generation of the inducible SNAP-tagged candidate cell lines, the SNAP-tag sequence was PCR-amplified from the inducible MCFT-SNAP vector with suitable restriction site overhangs. The inducible Sox2-SNAP cell line was generated from the pLVTR3G-Sox2-YPet (Deluz et al., 2016) by replacing the YPet sequence with the SNAP-tag sequence. For the remaining SNAP-tag fusion cell lines, the coding sequences of both the housekeeping proteins and transcription factors were PCR-amplified from E14 wild-type cDNA upon mRNA extraction and cDNA synthesis, using primers with suitable restriction site overhangs. The coding sequences and SNAP-tag sequence were ligated into the pLVTR3GMCS vector to generate the following constructs:

- pLVTR3G-Mlul-Sept7-SpeI-SNAP-Ascl
- pLVTR3G-Sall-Wdr43-SpeI-SNAP-Ascl
- pLVTR3G-Sall-Dstn-SpeI-SNAP-Ascl
- pLVTR3G-Sall-Msn-Ascl-SNAP-EcoRV
- pLVTR3G-Sall-Caprin1-Ascl-SNAP-EcoRV
- pLVTR3G-Sall-Srsf11-Ascl-SNAP-EcoRV
- pLVTR3G-Sall-Ybx1-Ascl-SNAP-EcoRV
- pLVTR3G-Sall-Orc6-Ascl-SNAP-EcoRV
- pLVTR3G-Sall-Ube2s-Ascl-SNAP-EcoRV
- pLVTR3G-Sall-Sox2-Ascl-SNAP-EcoRV
- pLVTR3G-Sall-Oct4-Ascl-SNAP-EcoRV
- pLVTR3G-Sall-Nanog-Ascl-SNAP-EcoRV
- pLVTR3G-Sall-Esrrb-Ascl-SNAP-EcoRV
- pLVTR3G-Sall-Klf4-Ascl-SNAP-EcoRV

To generate the inducible Sox2-, Oct4-, Nanog-, and Orc6-Halo cell lines, the pLVTR3G-Sox2-SNAP, pLVTR3G-Oct4-SNAP, pLVTR3G-Nanog-SNAP and pLVTR3G-Orc6-SNAP vectors were digested with Ascl and EcoRV to replace the SNAP-tag sequence by the Halo-tag sequence previously PCR amplified with the corresponding restriction site overhangs. This led to the generation of the following constructs:

- pLVTR3G-Sall-Sox2-Ascl-Halo-EcoRV
- pLVTR3G-Sall-Oct4-Ascl-Halo-EcoRV
- pLVTR3G-Sall-Nanog-Ascl-Halo-EcoRV
- pLVTR3G-Sall-Orc6-Ascl-Halo-EcoRV

For the FRET experiments, an inducible nuclear sfGFP and an inducible mCherry-sfGFP timer were generated. For the inducible nuclear sfGFP, the sfGFP sequence was amplified with Sall and Ascl restriction site overhangs and the SNAP-NLS-NLS was amplified from the MCFT-SNAP-PEST using primers containing Ascl and EcoRV restriction site overhangs. The pLVTR3G-Sox2-SNAP vector was then digested with Sall and EcoRV to remove the Sox2-SNAP sequence and the sfGFP and SNAP-NLS-NLS

were ligated into the digested vector. For the mCherry-sfGFP timer, the mCherry sequence was PCR-amplified with restriction site overhangs for Sall and Ascl and the sfGFP sequence was amplified with restriction site overhangs for Ascl and EcoRV. Subsequently, the inducible long-lived MCFT (pLVTRE3G-mOrange2-sfGFP-SNAP-NLS) was digested with Sall and EcoRV and mCherry and sfGFP sequences were ligated into the vector, which led to the generation of a pLVTRE3G-mCherry-sfGFP-SNAP-NLS vector.

For the inducible sfGFP-FLuc-NLS-PEST cell line, the sfGFP sequence was PCR-amplified with restriction site overhangs for Sall and XbaI and the FLuc-NLS-PEST sequence was PCR-amplified with restriction site overhangs for XbaI and Ascl. The two fragments were subsequently ligated into the pLVTRE3GMCS vector.

To generate a pLVTRE3G-Adrm1 overexpression construct, the Adrm1 sequence was PCR amplified from the pCMV6-Entry-Adrm1 plasmid (OriGene, MR206404) with restriction site overhangs for Sall and Ascl and ligated into the pLVTRE3G vector.

### Production of lentiviral vectors and generation of stable cell lines

HEK293T cells were seeded at a density of 45,000 cells/cm<sup>2</sup> and transfected using calcium phosphate one day after seeding. Cells were co-transfected with PAX2 (envelope), MD2G (packaging), and the lentiviral construct of interest and concentrated 120-fold by ultracentrifugation as described previously (Suter et al., 2006). Target E14 or 3T3 cells were seeded at a density of 13,000/cm<sup>2</sup> in a 24-well plate and transduced with 50  $\mu$ L of concentrated lentivirus. For all dox-inducible cell lines, cells were first transduced with the pLV-pGK-rtTA3G-IRES-Bsd construct (Deluz et al., 2016), selected using 8  $\mu$ g/ml Blasticidin (ThermoFisher, A11139-03), transduced with the pLVTRE3G-construct of interest, and selected with puromycin (ThermoFisher, A11138-03) at 2  $\mu$ g/ml. For the dual SNAP/Halo-tag cell lines, cells were first transduced with the rtTA3G-IRES-Bsd and the pLVTRE3G-SNAP constructs of interest, and selected for 10 days. Subsequently, cells were transduced with the pLVTRE3G-Halo construct of interest, labeled with 100 nM TMR Halo ligand (Promega, G8251) and sorted for Halo-positive cells by fluorescence activated cell sorting (FACS) 4 – 6 days after transduction. 100,000 to 200,000 cells per cell line were sorted and outgrown in 100 mm cell culture dishes as polyclonal cell lines. Similarly, the inducible Adrm1/Sox2-SNAP and Adrm1/Orc6-SNAP cell lines were generated by first transducing cells with the rtTA3G-IRES-Bsd and pLVTRE3G-Adrm1 constructs and selecting with Blasticidin and Puromycin for 10 days. Subsequently, cells were transduced with the pLVTRE3G-Sox2-SNAP or the pLVTRE3G-Orc6-SNAP construct and sorted for SNAP-positive cells upon pulse-labeling with 12 nM of SNAP-Cell® 647-SiR dye (NEB, S9102S) by fluorescence activated cell sorting (FACS) 4 days after transduction.

For the generation of the CD-tagged endogenous protein library,  $1.5 \times 10^6$  cells were plated per 100 mm cell culture dishes and transduced with 6.67  $\mu$ L of concentrated pSTAR-SA-mOrange2-sfGFP-SD virus. The medium was replaced one day after transduction and cells were sorted by FACS three days after transduction. 0.05% of cells were found to be GFP-positive and the 0.01% of cells displaying the brightest GFP signal were sorted into 96-well plates as single cells and outgrown as monoclonal cell lines. In total, a library of 40 cell lines, each expressing a different protein tagged with the MCFT was generated. Of note, incomplete degradation of sfGFP in tandem fluorescent timers has been observed previously and could perturb the interpretation of fluorescence imaging (Khmelniskii et al., 2016). However, we would expect this to lead to a mismatch of the subcellular localization of the fluorescent signals of sfGFP and mOrange2 in a substantial number of tagged proteins, since protein localization signals are typically located within a single stretch of amino acids. We did not observe such mismatches for any of 40 our clones, suggesting the MCFT is not affected by incomplete degradation.

### Identification of insertion sites by 3' Rapid Amplification of cDNA Ends

Tagged protein identification was performed by 3' Rapid Amplification of cDNA Ends (3'RACE) as described previously (Sigal et al., 2007). Briefly, cells were grown up to confluences of 70% in 6-well plates and total RNA was extracted using an RNA miniprep kit (Sigma, RTN70-1KT). Subsequently, cDNA was synthesized using the superscript II reverse transcriptase (Invitrogen, 18064-014) with the following primer:

5'GCTCGCGAGCGCGTTTTAAACGCGCACGCGTTTTTTTTTTTTTTTTTTTTVN3'

Two nested PCR reactions were then performed using the following primers:

1<sup>st</sup> PCR:

Forward (within sfGFP sequence): 5'AGCTCGCCGATCACTATCAACAGAA3'

Reverse (within 3' adaptor sequence): 5' GCTCGCGAGCGCGTTTTAAAC3'

2<sup>nd</sup> PCR:

Forward (within sfGFP sequence): 5'CGACAACCACTACCTGAGTACCCAGAC3'

Reverse (within 3' adaptor sequence): 5'GCGTTTTAAACGCGCACGCGT3'

PCR products were purified after the 1<sup>st</sup> PCR reaction and run on an agarose gel after the 2<sup>nd</sup> PCR reaction. Bands were cut, gel-extracted, and sent for Sanger sequencing. In case of multiple bands, indicating multiple splice variants, all bands were cut and sent for sequencing separately.

### Time-lapse fluorescence microscopy

Fluorescence time-lapse imaging experiments were performed as previously described (Alber and Suter, 2018). Briefly, cells were seeded on 96-well plates coated with 5 ng/ $\mu$ L recombinant mouse or rat E-cadherin Fc chimera protein (E-cad-Fc, R&D systems, 748-EC-050 or 8144-EC-050) at densities of 30 000 cells/cm<sup>2</sup>.

For imaging of the CD-tagged protein library, the culture medium was replaced by FluoroBrite DMEM (ThermoFisher, A18967-01), supplemented with 10% ES cell-qualified fetal bovine serum, 2 mM sodium pyruvate, 1% non-essential amino acids, 1% penicillin/streptomycin, 2 mM L-glutamine, 100  $\mu$ M 2-mercaptoethanol, LIF, 3  $\mu$ M CHIR99021 and 0.8  $\mu$ M PD184352 24 h after cell seeding and cells were imaged using an InCell Analyzer 2200 (GE Healthcare Life Sciences) for 24-30 h with time intervals of 15 min (Objective: 20x, Laser power: 10%, Exposure: 300 ms for FITC, 500 ms for Cy3, live cell imaging settings: 5% CO<sub>2</sub> and 37°C).

For imaging of the dox-inducible SNAP-tag and SNAP/Halo-tag cell lines, 500 ng/ml doxycycline was added 7 h before imaging for the SNAP-tagged pluripotency transcription factors, and 24 h before imaging for the SNAP-tagged housekeeping proteins and the dual SNAP/Halo-tagged cell lines. 2 h before starting the time-lapse experiment, cells were pulse-labeled with 12 nM of SNAP-Cell® 647-SiR dye (NEB, S9102S) and 100 nM of Halo-Tag® TMR dye (Promega, G8251) and washed repeatedly, as described in (Alber and Suter, 2018). For pulse-labeling of the Sox2-SNAP/Oct4-Halo knockin cell line, concentrations of 12 nM of SNAP-Cell® 647-SiR dye and 5 nM of Halo-Tag® TMR dye were used. Subsequently, imaging medium was added (FluoroBrite DMEM supplemented as described above for ES cells, FluoroBrite DMEM supplemented with FBS and penicillin/streptomycin for 3T3 cells) and cells were imaged using an InCell Analyzer 2200 (GE Healthcare Life Sciences) for 12 - 20 h at time intervals for 15 min (Objective: 20x, Laser power: 10%, Exposure: 100 - 300 ms for Cy5, 50 - 100 ms for Cy3, live cell imaging settings: 5% CO<sub>2</sub> and 37°C).

### Image processing and analysis

#### Image processing

The acquired time-lapse fluorescence movies were collected as stacks in tiff format and further processed using the Fiji software (Schindelin et al., 2012). The background was subtracted from all the images in the stack using the Fiji background subtraction algorithm (rolling ball radius = 50 pixels).

#### Automated cell tracking and image quantification for full cell cycle analysis

For the analysis of the full cell cycle traces of the CD-tagged nuclear proteins (Figure 2), a semi-automated image analysis pipeline was used to quantify the integrated fluorescence intensities over the whole cell cycle (Bieler et al., 2014).

#### Manual cell tracking and image quantification from 5h before to 5h after cytokinesis

For the analysis of the synthesis and degradation rates before, during and after division (Figure 3), dividing cells were selected and manually quantified from 20 time frames (5 h) before to 20 time frames (5 h) after division. To do so, a circle or polygon was drawn around the cell of interest for each time frame, its area and mean intensity were measured and its integrated intensity was calculated over the course of the movie for both fluorescence channels:

$$I_{\text{cell}} = \text{Mean}_{\text{cell}} * \text{Area}_{\text{Cell}}$$

Subsequently, the local background was estimated by drawing a circle close to the cell of interest (but excluding any cellular signal) for each time frame and the integrated background intensity of the cell was estimated:

$$I_{\text{BG}} = \text{Mean}_{\text{BG}} * \text{Area}_{\text{Cell}}$$

Finally, the background-subtracted intensity over time was calculated for each single cell:

$$I_{\text{Cell-BG}} = I_{\text{Cell}} - I_{\text{BG}}$$

Note that we summed up the intensities of both daughter cells in order to determine changes of synthesis and degradation before and after division for the same number of gene copies (2 tagged alleles).

#### Estimation of protein degradation rates using the SNAP-tag

Degradation rates during division were measured using the SNAP-tag fluorescence decay movies of 7 inducible SNAP-tagged proteins of interest. Dividing cells were selected manually and integrated fluorescence intensities were analyzed from 5 h before to 5 h after division as described previously for the MCFT-tagged proteins. The integrated fluorescence intensities at the time-point of division (first time frame at which the daughter cells were separated) were set as time  $t = 0$  and normalized to 1. The cell averaged fluorescence decay was calculated to determine transient changes in degradation during division.

Single cell protein half-lives of the SNAP/Halo-tagged proteins (Figures 4–6) were calculated as described previously (Alber and Suter, 2018). Briefly, integrated fluorescence intensities were measured over 50 time frames (12.5 h), summing up the intensities of the daughter cells in case of cell divisions. Analyzed cells were picked randomly, such that divisions took place at different time-points for all individual traces. Next, fluorescence intensity traces were normalized to the intensity of the first frame and a curve fitting was performed in MATLAB, using the following equation:

$$F(t) = e^{-bt}$$

Where  $F(t)$  is the fluorescence intensity over time and  $b$  is the decay rate. The single cell half-lives were then calculated as follows:

$$T_{1/2} = \ln(2)/b$$

### Immunofluorescence experiments

To correlate protein degradation rates and expression levels of proteasome components in single cells, protein half-lives were calculated by monitoring the fluorescence decay of the SNAP-tagged protein of interest as described above. After time-lapse imaging, cells were immediately fixed in PBS + 2% paraformaldehyde for 30 min, permeabilized in 0.5% Triton for 30 min and blocked in PBS + 5% FBS for 30 min. Cells were incubated overnight with the primary antibody, diluted in PBS + 5% FBS. The primary antibody used and their concentrations were as following: anti ADRM1 antibody 1/200 (1  $\mu$ g/ml) (sc-376221, Santa Cruz Biotechnology), anti Tbp7 antibody 1/100 (ab139184, abcam), anti Proteasome 20S alpha 2 1/100 (ab109525, abcam). Next, cells were washed 2x in PBS and incubated with a fluorescently-labeled secondary antibody (1/1000) in PBS + 5% FBS for 1 h. Cells were then washed with 3x with PBS-Tween 0.1% and incubated with 1  $\mu$ g/ml DAPI. Finally, cells were washed 3x with PBS-Tween 0.1% and left in PBS. Fixed and stained cells were re-imaged, using the same xy-coordinates as for the fluorescence decay imaging. Cells for which the SNAP fluorescence decay had been acquired previously were re-identified in the immunofluorescence images and the integrated fluorescence intensity of the antibody was quantified as described previously. In case of divisions, the average integrated intensity of both daughter cells was calculated.

### Modeling the mammalian cell-optimized tandem fluorescent timer (MCFT)

The mathematical model used to infer the synthesis and degradation rates from the fluorescence traces obtained from the MCFT relies on the differential maturation dynamics of the sfGFP and mOrange2 proteins. To model the maturation dynamics of the MCFT, we assumed as previously (Barry et al., 2016; Khmelinskii et al., 2012) that the two fluorophores present on the same polypeptide mature independently at rate  $m_G$  and  $m_R$  (Figure 1B). Thus, we can model the dynamics of the mature green and red proteins using the four variables defined in Figure 1C as follows:

$$\begin{aligned} \dot{B}_G &= s - (m_G + k)B_G \\ \dot{G} &= m_G B_G - kG \\ \dot{B}_R &= s - (m_R + k)B_R \\ \dot{R} &= m_R B_R - kR \end{aligned} \quad (1)$$

Here,  $B_G$  stands for the pool of proteins with an immature (black) sfGFP, which is synthesized at a rate  $s$ . The immature sfGFP then matures into the green ( $G$ ) fluorescent form. A corresponding set of equations describes the mOrange2 fluorophore, i.e., the immature form of the mOrange2 ( $B_R$ ) is converted to a mature form ( $R$ ) at a maturation rate  $m_R$ . Note that in this formulation, the synthesis  $s$  commonly acts on both  $B_G$  and  $B_R$ , and the degradation rate  $k$  does not depend on the maturation state of the fluorophores. The total level of the protein  $T$  is given by  $T = B_G + G = B_R + R$ .

### Estimating the fluorescence correction factor $\alpha$

To later compare the measured fluorescence levels with the model predictions, an empirically determined scale factor  $\alpha$  (applied to mOrange2) is needed to compensate for the different optical properties of the two fluorescent proteins and the imaging settings of the two channels.

To estimate  $\alpha$ , we used a condition where the levels of matured sfGFP and mOrange2 proteins are very similar. In order to achieve this, we used a doxycycline (dox)-inducible construct expressing a long-lived version of the MCFT that we induced for 24 h before stopping the induction. In this condition the measured green to red fluorescence ratio  $G/R$  is expected to converge to  $\alpha$ , as demonstrated in a simulation (Figures S6A and S6B). Guided by this simulation we decided to quantify  $\alpha$  55 h after stopping the induction since the level of both the sfGFP and mOrange2 were still detectable and the  $G/R$  ratio reached a stable value of  $\alpha$  (Figure S6B).

We estimated the  $G/R$  ratio from 30 different individual cells taken from three different fields of view using a standardized set of imaging parameters and on the same microscope that was used throughout the entire study. We also validated that the amount of dox, and consequently the intensity level of the MCFT, did not have any impact on the estimated  $\alpha$  (Figure S6C). We see that the estimated  $G/R$  ratio (i.e.,  $\alpha$ ) is tightly centered on 0.6, meaning that in our system, the sfGFP protein has an intensity corresponding to 60% of the mOrange2 protein. Consequently, for all the modeling performed in this study, we used a value of  $\alpha = 0.6$ .

### Estimating the sfGFP maturation time

To validate the short maturation kinetics of sfGFP, we took advantage of the SNAP-tag (Figure S1D), which is not dependent on fluorophore maturation, and we also generated a cell line allowing dox-inducible expression of the fast-folding Firefly luciferase (Fluc) fused to sfGFP (Kolb et al., 1994; Molina et al., 2013). We seeded sfGFP-Fluc and MCFT-SNAP-PEST cells on E-cadherin and induced with 500 ng/ml doxycycline shortly before onset of imaging. sfGFP-Fluc cells were imaged with a luminescence microscope (LV200, Olympus) and a fluorescence microscope (Cell Xcellence, Zeiss). MCFT-SNAP-PEST cells were incubated with 24 nM of SiR-647 SNAP dye that was left in the medium, and imaged with a fluorescence microscope (Cell Xcellence, Zeiss). We analyzed integrated luminescence and fluorescence traces from the time frame at which a signal appeared (2.5 h after addition

of dox) and compared the rate of green fluorescence increase upon dox induction to i) the rate of luminescence increase in the inducible sfGFP-Fluc cell line, and ii) the rate of SNAP SiR647 signal increase in the MCFT-SNAP-PEST cell line. The green fluorescence increase was indistinguishable from the increase in Fluc signal or SNAP fluorescence (Figure S6D). This suggests that the sfGFP maturation rate lies within the same range as the folding times of the SNAP-tag and firefly luciferase, in line with the measured sfGFP maturation half-time of 5 – 14 min (Balleza et al., 2018; Khmelinskii et al., 2012).

### Estimating the mOrange2 maturation time

To model the MCFT using the set of differential equations (ref. Equation 1), we also needed to estimate the mOrange2 maturation time ( $m_R$ ). To achieve this, we compared the half-life estimations made with the MCFT to an independent approach using the SNAP-tag approach described (Figure S1D).

Using the half-life estimations obtained for seven proteins (CAPRIN1, DESTRIN/DSTN, MSN, SEPTIN7, SRSF11, WDR43, and YBX1, see Figure 4B) with the SNAP-tag approach as our gold-standard, we determined  $m_R$  that would give half-life estimates that closely match the values retrieved from our gold standard. For this we used the MCFT data acquired around division for the seven proteins (Figure 3) in combination with our fitting approach around cell division (see section below) to estimate the half-life before (bD) and after division (aD).

We reasoned that the optimal  $m_R$  would lead to a slope as close as possible to 1 when comparing the half-lives of the gold-standard with the ones retrieved from the MCFT. To find the optimal  $m_R$ , we tested maturation half-time values from 1 h to 18.5 h with 0.5 h increment. For every  $m_R$ , we obtained half-lives for all seven proteins from our MCFT that we compared to those obtained from the SNAP-tag using a linear relationship with no intercept. From this analysis we found that the optimal  $m_R$ , i.e., the one yielding a distribution of slopes centered on one, corresponds to a maturation half-time of 8.5 h (Figure S6E).

### Quantification of FRET effects in the MCFT

We quantified putative FRET effects between the sfGFP and mOrange2 by fluorescence lifetime imaging (FLIM), using an SP8 FLIM microscope (Leica). We compared the fluorescence lifetime of sfGFP in a cell line expressing nuclear sfGFP alone (inducible sfGFP-SNAP-NLS) to its lifetime in the two inducible timer cell lines MCFT-SNAP and MCFT-SNAP-PEST (Figure 1), and in one additional cell line from our endogenous MCFT-tagged protein library (Snmp200). sfGFP fluorescence lifetime was quantified and averaged for three cells per cell line, with 1000 – 2500 kiloCounts being acquired per cell. We found that the FRET effect between sfGFP and mOrange2 is negligible (average FRET for the three cell lines tested = 1.25%) (MCFT-SNAP-PEST = -0.26%, MCFT-SNAP = -0.79%, and Snmp200-MCFT = 4.8%). As a control we used an inducible mCherry-sfGFP timer, for which we found a FRET of 15.5%, in line with the previously reported value of 17.3% (Khmelinskii et al., 2012).

### Fitting the MCFT during interphase

We modeled the MCFT to fit the red and green intensities during interphase (Figure 2) using the set of equations described in Equation 1, but with time-dependent rates  $s(t)$  and  $k(t)$ :

$$\begin{aligned} \dot{B}_G &= s(t) - (m_G + k(t))B_G \\ \dot{G} &= m_G B_G - k(t)G \\ \dot{B}_R &= s(t) - (m_R + k(t))B_R \\ \dot{R} &= m_R B_R - k(t)R \end{aligned} \quad (2)$$

We opted to use a linear functions for  $s(t)$  and  $k(t)$  to keep the number of parameters low in our model. We therefore used two synthesis rates ( $s_{G1}$  and  $s_{G2}$ ) and two degradation rates ( $k_{G1}$  and  $k_{G2}$ ), the first at the beginning (G1) and the second at the end (G2) of the cell cycle (Figure S6H):

$$\begin{aligned} s(t) &= s_{G1} + \left( \frac{s_{G2} - s_{G1}}{l} \right) t \\ k(t) &= k_{G1} + \left( \frac{k_{G2} - k_{G1}}{l} \right) t \end{aligned} \quad (3)$$

where  $l$  corresponds to the cell cycle duration (in hours) and is specific to each cell trace.

The full set of parameters  $\Theta = \{T_0, BG_0, BR_0, s_{G1}, s_{G2}, k_{G1}, k_{G2}\}$  now also includes the three initial conditions  $BG_0 = BG(0)$ ,  $BR_0 = BR(0)$  and  $T_0 = T(0)$  ( $T = B_G + G = B_R + R$  is the total protein abundance) in addition to the two synthesis and degradation rates. We then maximized the likelihood of the observed green ( $G_0$ ) and red ( $R_0$ ) signals given the parameters  $\Theta$  (Equation 4), using the previously determined value of  $\alpha = 0.6$ , as well as the green and red maturation rates  $m_G$  and  $m_R$  (corresponding to maturation half-times of 5 min for sfGFP and 8.5 h for mOrange2). For every new set of parameters  $\Theta$ , we simulated green ( $G_s$ ) and red ( $R_s$ ) signals from the second time frame after cell division ( $i = 1$ ) to one hour before cell division ( $i = n$ ).

Exploratory analysis showed that a multiplicative noise model is suitable, which led us to use the following likelihood function:

$$\begin{aligned}\hat{\Theta} &= \operatorname{argmax}_{\Theta} \log p(G_o, R_o | \Theta) \\ p(G_o, R_o | \Theta) &= \prod_{i=1}^n f\left(\frac{G_{oi} - G_{si}}{G_{si}}\right) \prod_{i=1}^n f\left(\frac{\alpha^{-1}R_{oi} - R_{si}}{R_{si}}\right) \\ f(x) &= \frac{1}{\sigma\sqrt{2\pi}} e^{-\frac{x^2}{2\sigma^2}}\end{aligned}\quad (4)$$

with  $\sigma = 0.1$ .  $G_{oi}$ ,  $G_{si}$ ,  $R_{oi}$ ,  $R_{si}$  stands for green (G) and red (R) traces, observed (o) or simulated (s) at time point  $i$ .

We applied this optimization procedure to all individual traces of all 6 nuclear MCFT-tagged proteins. In [Figure S6H](#) we show the best fit of one individual trace. We used the optim function in R with the box constraints approach (L-BFGS-B) for optimizing all parameters ( $\Theta$ ). Standard errors of the optimal  $\Theta$  parameters were obtained by inverting the negative Hessian matrix.

### Validating synthesis and degradation retrieval during interphase

To test the analysis during interphase, we simulated traces to mimic the real traces obtained using the MCFT. To evaluate how much noise should be added to our simulated traces, we used the traces obtained around division from all 40 proteins and estimated relative noise as follows:  $(G_{oi} - \tilde{G}_i)/\tilde{G}_i$  and  $(R_{oi} - \tilde{R}_i)/\tilde{R}_i$ , where  $\tilde{G}_i$  and  $\tilde{R}_i$  were obtained from smoothing  $G_{oi}$  and  $R_{oi}$  (using the standard lowess function in R, [Figure S6F](#)). These relative noise levels were found to be fairly homogeneous across all the proteins ([Figure S6G](#)).

Simulating realistic traces during interphase required four rates ( $s_{G1}$ ,  $s_{G2}$ ,  $k_{G1}$ , and  $k_{G2}$ ) in addition to the timer parameters ([Figure S6H](#)). We used parameter values retrieved around division ([Figure 3](#)). G2 parameters were estimated before division (bD), while G1 for parameters estimated after division (aD) for the individual cells. An example of the simulated traces obtained from the gene GRB2 are shown in [Figure S6I](#). To evaluate if our approach could retrieve the simulation parameters we calculated the relative error between the simulated and retrieved parameters ([Figure S6J](#)). Overall, for most parameters and over all 40 realistic simulations obtained from our 40 genes (i.e., 20 simulated traces from 40 genes), the relative error corresponded to 5% (0.05) of the simulated parameters ([Figure S6K](#)).

### Fitting the MCFT around cell division

When studying protein dynamics around cell division with the MCFT, we faced challenges, notably since mitosis is short ( $\sim 1$  h) relative to the remaining of the cell cycle, and also because cells detach during this period, introducing artifacts in the recorded fluorescence signals. Thus, we could not directly rely on the signal during division to infer protein dynamics, but used the flanking signals (not influenced by detachment) to constrain the dynamics during division (schematized in [Figure S6L](#)). To keep the model parsimonious we modeled the entire signal around division using piecewise constant degradation and synthesis rates, i.e., one ( $s$ ,  $k$ ) pair for every interval (before division (bD), during division (D), after division (aD)). Thus,  $s(t)$  and  $k(t)$  are given by:

$$\begin{aligned}s(t) &= \begin{cases} s_{bD} & \text{if } t < -45 \text{ min} \\ s_D & \text{if } -45 \leq t < 45 \text{ min} \\ s_{aD} & \text{if } t \geq 45 \text{ min} \end{cases} \\ k(t) &= \begin{cases} k_{bD} & \text{if } t < -45 \text{ min} \\ k_D & \text{if } -45 \leq t < 45 \text{ min} \\ k_{aD} & \text{if } t \geq 45 \text{ min} \end{cases}\end{aligned}\quad (5)$$

The full set of parameters  $\Theta = \{T_0, BG_0, BR_0, s_{bD}, s_D, s_{aD}, k_{bD}, k_D, k_{aD}\}$  now also includes the three initial conditions  $BG_0 = BG(0)$ ,  $BR_0 = BR(0)$  and  $T_0 = T(0)$  ( $T = B_G + G = B_R + R$  is the total protein abundance) corresponding to the levels at the beginning of the bD interval. Also, in G1 we summed the signals of the two daughter cells to study the dynamic of the labeled protein pool per fixed number (two) of tagged alleles. We then maximized the likelihood of the green ( $G_o$ ) and red ( $R_o$ ) observed signals given the parameters  $\Theta$  ([Equation 4](#)) ([Figure S6L](#)).

### Validating synthesis and degradation retrieval around cell division

For validation, we simulated individual traces using parameters  $s_{bD}$ ,  $s_D$ ,  $s_{aD}$ ,  $k_{bD}$ ,  $k_D$ , and  $k_{aD}$  (see [Figures S6L](#) and [S6M](#)) and evaluated how precisely our approach is able to retrieve those parameters. We simulated green and red traces using a realistic set of heterogeneous parameters (i.e., different sets of synthesis and degradation rates) to mimic cell traces around division. For this we used the median of the inferred parameters for the 40 genes in our library. We show an example of simulated traces using the median parameters for SF3B1 as well as the distributions of the retrieved parameters ([Figures S6M](#) and [S6N](#)). Overall, for most parameters and over all 40 realistic simulations obtained from our 40 genes (i.e., 20 simulated traces from 40 genes), the relative error corresponded to 5% (0.05) of the simulated parameters with a 5% increase for parameters inferred during division ([Figure S6O](#)).

### Analysis of correlations in synthesis and degradation rates

To assess the impact of correlations between the synthesis ( $s$ ) and the degradation rates ( $k$ ) on the mean expression level and the coefficient of variation (standard deviation/mean) (Figures 4E, 4F, and S4D–S4F), we simulated traces using the MCFT model (Figure 1C). We simulated a first set of traces using the estimated degradation and synthesis rates in all individual traces, and a second set of traces in which we broke the observed correlations by randomly shuffling the degradation and synthesis rates between the cells. We used the simulated traces to estimate protein level (Figure S4E) and the coefficient of variation (Figures 4E, 4F, and S4F) at 50% of the steady state ( $s/k$ ).

### QUANTIFICATION AND STATISTICAL ANALYSIS

Statistical analysis was performed using the R software. In Figures 3A, 3D, S3A, and S3B, we used a one-sided Wilcoxon test to determine if the accumulation rates (slopes, Figure 3A) and levels (Figure 3D) and the integrated green fluorescence intensity increased or decreased around division considering a Benjamini-Hochberg adjusted  $p < 0.05$  to be significant. For the Pearson correlations (Figures 4–6), the correlation ( $R$ ), determination ( $R$  squared) and  $p$  values were determined (Table S3).  $p < 0.05$  was considered statistically significant. For monitoring the changes in half-life upon ADRM1 overexpression (Figure 6D) a two-tailed Student's  $t$  test was performed and  $p$  values  $< 0.05$  were considered significant.

### DATA AND SOFTWARE AVAILABILITY

Original imaging data have been deposited to Mendeley Data and can be accessed using the following link: <https://data.mendeley.com/datasets/sgyzkr223j/1>